Modeling of localized phase transformation in pseudoelastic shape memory alloys accounting for martensite reorientation[†]

Mohsen Rezaee-Hajidehi[a,*]

[a] *Institute of Fundamental Technological Research (IPPT), Polish Academy of Sciences,*
Pawińskiego 5B, 02-106 Warsaw, Poland.

Abstract

A reliable prediction of the pseudoelastic behavior necessitates the involvement of martensite reorientation in the model. This is important not only under non-proportional loading but in general when the phase transformation proceeds in a localized manner, which results in complex local deformation paths. In this work, an advanced model of pseudoelasticity is developed within the incremental energy minimization framework. A novel enhancement of the model over its original version lies in the formulation of a suitable rate-independent dissipation potential that incorporates the dissipation due to martensitic phase transformation and also due to martensite reorientation, thus yielding an accurate description of the inelastic transformation strain. The finite-element implementation of the model relies on the augmented Lagrangian treatment of the non-smooth incremental energy problem. Thanks to the micromrophic regularization, the related complexities are efficiently handled at the local level, leading to a robust finite-element model. Numerical studies highlight the predictive capabilities of the model. The characteristic mechanical behavior of NiTi tubes under non-proportional tension–torsion and the intricate transformation evolution under pure bending are effectively captured by the model. Additionally, a detailed analysis is carried out to elucidate the important role of martensite reorientation in promoting the striations of the phase transformation front.

Keywords: Shape memory alloys; Phase transformation; Martensite reorientation; Strain localization, Finite-element method

---

1. Introduction

The reversible evolution of martensitic microstructure is the underlying mechanism behind the unique properties of shape memory alloys (SMAs), namely pseudoelasticity and shape memory effect (Bhattacharya, 2003). When SMA is subjected to mechanical loading, a biased martensitic microstructure develops that accommodates those martensite variants with crystallographic structures favorable to the loading direction (Miyazaki et al., 1989; Duerig et al., 2013). Upon altering the direction of the applied load within a non-proportional loading path,

---

[*] Corresponding author.
Email address: `mrezaee@ippt.pan.pl` (Mohsen Rezaee-Hajidehi)

[†] Dedicated to the memory of Giovanni Minafò, a young scientist who passed away on 23rd December 2023.

[†] Published in *Eur. J. Mech. A Solids*, 2024, doi: 10.1016/j.euromechsol.2024.105376

a different set of variants becomes preferable, and this leads to the phenomenon of *variant reorientation*. In pseudoelastic SMAs, the process of variant alignment/reorientation occurs in conjunction with austenite–martensite phase transformation. Various experimental studies have shown the complex transformation behavior resulting from the simultaneous evolution of transformation and reorientation under non-proportional loading conditions and have identified reorientation as a major inelastic deformation contributor (e.g., Lim and McDowell, 1999; Sun and Li, 2002; Bouvet et al., 2002; McNaney et al., 2003; Helm and Haupt, 2003; Grabe and Bruhns, 2009; Song et al., 2014).

To date, a plethora of macroscopic models has been developed to capture the complex behavior of polycrystalline SMAs. The corresponding literature is quite rich, and a thorough review is beyond the scope of this discussion; interested readers are directed to Lagoudas et al. (2006); Saleeb et al. (2011); Auricchio et al. (2014); Cissé et al. (2016); Alsawalhi and Landis (2022). Within the phenomenological framework, appropriate internal variables are defined and the corresponding evolution laws are formulated to represent faithfully the behavior of the material without a direct link to the micromechanical considerations. Typically, a scalar-type internal variable, i.e., the volume fraction of martensite, and a tensorial one, representing the transformation strain, are adequate to characterize the inelastic deformation (Luig and Bruhns, 2008). When dealing with unidirectional loading only, the kinematics of the phase transformation can be considerably simplified, allowing to confidently assume a fixed and predetermined transformation strain, as for instance in phase-field-type approaches (He and Sun, 2010; Wendler et al., 2017). On the contrary, in order to address arbitrary multiaxial loading conditions, a proper depiction of the material's behavior relies upon a rigorous formulation of the transformation strain. Such a formulation must effectively account for martensite variant reorientation and its interaction with the phase transformation, and this is only achieved when the energetic cost associated with the evolution of the internal variables is correctly embedded into the model (Sedlak et al., 2012). In the present work, the model is based on the incremental energy minimization approach. Accordingly, a physically meaningful formulation of the evolution equations demands a suitable dissipation potential that properly penalizes the changes in the martensite volume fraction and, more crucially, the transformation strain. It is generally accepted that, under isothermal conditions, SMAs exhibit macroscopically a *rate-independent* hysteresis behavior (Sun and He, 2008). Important to highlight is thus the non-smoothness of the rate-independent dissipation potential that, along with the equality/inequality constraints on the internal variables, may compromise the robustness of the resulting computational model if not handled carefully.

While devising sophisticated constitutive models that incorporate various physical aspects and coupling mechanisms is undeniably crucial, implementing the models into the finite-element framework is a necessary next step for tackling problems of practical relevance. This necessity arises since the structural response of SMA specimens is greatly influenced by the transformation localization and propagation, and is substantially different than the intrinsic material response (Hallai and Kyriakides, 2013). Stress-induced martensitic transformation in pseudoelastic NiTi under uniaxial tension serves as a typical example of localized transformation that has been extensively studied both experimentally (e.g., Shaw and Kyriakides, 1997; Zhang et al., 2010; Bechle and Kyriakides, 2014) and numerically (e.g., Jiang et al., 2017b; Rezaee-Hajidehi et al., 2020; Yu and Landis, 2023). A rich variety of inhomogeneous transformation patterns has been also reported for NiTi tubes under more involved loading conditions, such as bending (Bechle and Kyriakides, 2014; Reedlunn et al., 2014) and combined tension–torsion (Sun and Li, 2002; Reedlunn et al., 2020). Moreover, it is important to note that the emergence of localization alters significantly the local deformation process, resulting in material points experiencing complex non-proportional stress/strain paths under *nominally* proportional macroscopic loading (Reedlunn et al., 2020).

A suitable finite-element model is thus the one that, beside featuring an advanced constitutive material formulation, is able to treat the transformation localization effects. Special strategies ought to be employed in order to overcome the ill-posed problem of localization instability, which is led by a softening-type behavior in the material response. A common strategy involves enhancing the model, more specifically, the free energy function, with the gradient of the internal variable (Rezaee Hajidehi and Stupkiewicz, 2018). Here, the primary challenge is to come up with a robust finite-element implementation of the gradient-enhanced model, in particular, in view of resolving the localization and propagating interfaces, which necessitates adequately fine mesh densities and incurs high computational costs. Indeed, this challenge, together with the complexities inherent in the underlying constitutive equations, pose significant obstacles to the practical application of the existing models.

The model in this study originates from the model of pseudoelasticity proposed by Stupkiewicz and Petryk (2013), which has the following important characteristics: (i) it is based on the finite-deformation kinematics, (ii) its constitutive description involves tension–compression asymmetry and transverse isotropy of the transformation strain, (iii) it is formulated within the incremental energy minimization framework, and (iv) an augmented Lagrangian approach is utilized to satisfy the inequality constraints on the martensite volume fraction and to treat the non-smoothness of the rate-independent dissipation potential. The latter was deemed essential for a robust and efficient finite-element implementation. In light of the innate properties of the original model, its gradient-enhanced version was later developed and successfully applied to study the problem of transformation evolution in NiTi specimens under uniaxial tension and combined tension–torsion (Rezaee-Hajidehi et al., 2020; Rezaee-Hajidehi and Stupkiewicz, 2021b, 2023). On the debit side, a major simplification of the model lies in the form of the dissipation potential which solely penalizes the evolution of the martensite volume fraction, i.e., it only considers the dissipation due to phase transformation, while neglecting the energetic cost associated with martensite variant reorientation. As a consequence, the application of the model is limited to predominantly proportional loading conditions. To address this limitation, an extended form of the dissipation potential that incorporates the contribution of martensite reorientation is formulated in this work. It is to be remarked that deriving a mathematically consistent formulation that satisfies the general requirements of a rate-independent dissipation potential (specifically, being a positively homogeneous function of degree one in the rate of the internal variables, see more details in Stupkiewicz and Petryk (2013)) is rather straightforward. The main difficulty, however, resides in a proper computational treatment that maintains the robustness of the resulting finite-element model. This is accomplished here by generalizing the augmented Lagrangian approach, which marks the novelty of the present work in terms of the model development.

The remainder of this paper is organized as follows. Section 2 presents the model formulation. The particular emphasis of this section is on the choice of the dissipation potential, as elaborated in Section 2.4. The description of the finite-element model is provided in Section 3. Of prime importance in this section are the augmented Lagrangian functions that are tailored to the specific requirements of the present implementation. Section 4 is devoted to the finite-element studies. Three different scenarios are considered, each reflecting a different key aspect of incorporating the dissipation due to martensite reorientation into the model, and all intrinsically connected with the phase transformation localization/propagation.

2. Model formulation

This section is devoted to the description of the model formulation. The kinematics and the gradient-enhanced Helmholtz free energy function are identical to those in the previous version of the model (Rezaee-Hajidehi et al., 2020). The related equations are recapitulated in Sections 2.1 and 2.2, respectively. The incremental energy minimization framework is briefly outlined in Section 2.3. In Section 2.4, a detailed discussion is provided regarding the choice of the dissipation potential. A novel dissipation potential that accounts for martensitic transformation and reorientation is then adopted for the finite-element studies, which are reported in Section 4.

2.1. Kinematics

The kinematics of the model are formulated within the finite-deformation theory and are summarized below.

- Deformation gradient $\boldsymbol{F} = \nabla\boldsymbol{\varphi}$, with $\boldsymbol{\varphi}$ as the reference–current deformation mapping, is the primary kinematic quantity and is decomposed, in a multiplicative manner, into the elastic part $\boldsymbol{F}^{\mathrm{e}}$ and the transformation part $\boldsymbol{F}^{\mathrm{t}}$,

$$\boldsymbol{F} = \boldsymbol{F}^{\mathrm{e}}\boldsymbol{F}^{\mathrm{t}}. \tag{1}$$

- Two internal variables characterize the material state: the transformation strain $\boldsymbol{e}^{\mathrm{t}}$ and the martensite volume fraction η. The present model postulates that the transformation strain $\boldsymbol{e}^{\mathrm{t}}$ is purely deviatoric, thus $\mathrm{tr}(\boldsymbol{e}^{\mathrm{t}}) = 0$.

- Upon applying the polar decomposition, the transformation deformation gradient $\boldsymbol{F}^{\mathrm{t}}$ is represented in terms of a symmetric stretch tensor $\boldsymbol{U}^{\mathrm{t}}$ and a rotation tensor $\boldsymbol{R}^{\mathrm{t}}$, given by $\boldsymbol{F}^{\mathrm{t}} = \boldsymbol{R}^{\mathrm{t}}\boldsymbol{U}^{\mathrm{t}}$. The transformation stretch tensor $\boldsymbol{U}^{\mathrm{t}}$ is then expressed in the following exponential form,

$$\boldsymbol{U}^{\mathrm{t}} = \exp(\boldsymbol{e}^{\mathrm{t}}), \tag{2}$$

while the specification of the rotation $\boldsymbol{R}^{\mathrm{t}}$ is unnecessary, given the assumption of elastic isotropy, see Eq. (10). Clearly, in view of $\mathrm{tr}(\boldsymbol{e}^{\mathrm{t}}) = 0$, Eq. (2) implies $\det \boldsymbol{U}^{\mathrm{t}} = 1$. Moreover, the reference (stress-free) austenitic state is described by $\boldsymbol{F}^{\mathrm{t}} = \boldsymbol{U}^{\mathrm{t}} = \boldsymbol{I}$.

- It is assumed that the transformation strain $\boldsymbol{e}^{\mathrm{t}}$ is defined as a product of the volume fraction η and the transformation strain of fully-oriented martensite $\bar{\boldsymbol{e}}^{\mathrm{t}}$ (which is hereafter referred to as 'limit transformation strain'), viz.,

$$\boldsymbol{e}^{\mathrm{t}} = \eta \bar{\boldsymbol{e}}^{\mathrm{t}}. \tag{3}$$

- The variables η and $\bar{\boldsymbol{e}}^{\mathrm{t}}$ satisfy the following constraints,

$$0 \leq \eta \leq 1, \quad \bar{\boldsymbol{e}}^{\mathrm{t}} \in \bar{\mathcal{P}} = \{\bar{\boldsymbol{e}}^{\mathrm{t}} : g(\bar{\boldsymbol{e}}^{\mathrm{t}}) = 0\}, \tag{4}$$

  where $\eta = 0$ and $\eta = 1$ characterize, respectively, the pure austenite and pure martensite phases, and $g(\bar{\boldsymbol{e}}^{\mathrm{t}}) = 0$ defines the surface of the admissible limit transformation strains.

- The function $g(\bar{\boldsymbol{e}}^{\mathrm{t}})$ is capable of describing tension–compression asymmetry and transverse isotropy. It is defined in terms of the invariants I_k of the limit transformation strain tensor $\bar{\boldsymbol{e}}^{\mathrm{t}}$,

$$I_2 = -\frac{1}{2} \mathrm{tr}(\bar{\boldsymbol{e}}^{\mathrm{t}})^2, \quad I_3 = \det \bar{\boldsymbol{e}}^{\mathrm{t}}, \quad I_4 = \boldsymbol{m} \cdot \bar{\boldsymbol{e}}^{\mathrm{t}} \boldsymbol{m}. \tag{5}$$

  Note that I_4 serves as a mixed invariant of the tensor $\bar{\boldsymbol{e}}^{\mathrm{t}}$ and the vector $\boldsymbol{m}$ which indicates the axis of transverse isotropy. The function $g(\bar{\boldsymbol{e}}^{\mathrm{t}})$ is formulated as

$$g(\bar{\boldsymbol{e}}^{\mathrm{t}}) = \Big[(-I_2)^{3/2} - bI_3 - cI_4^3\Big]^{1/3} - a, \tag{6}$$

  where

$$a = \epsilon_{\mathrm{T}} \Big[\frac{3\sqrt{3}}{4(1+\alpha^3)}\Big]^{1/3}, \quad b = \frac{\sqrt{3}}{6} \frac{9\alpha^3\beta^3 - 7\alpha^3 + 7\beta^3 - 9}{(1+\alpha^3)(1+\beta^3)}, \quad c = \frac{2\sqrt{3}}{3} \frac{\alpha^3 - \beta^3}{(1+\alpha^3)(1+\beta^3)}. \tag{7}$$

  The parameters α, β and ϵ_{T} characterize, respectively, the tension–compression asymmetry ratio, the degree of transverse isotropy and the maximum transformation strain attainable in uniaxial tension.

2.2. Free energy function

The gradient-enhanced Helmholtz free energy function ϕ is composed of the following contributions: the chemical energy ϕ_{chem}, the elastic strain energy ϕ_{el}, the interaction energy ϕ_{int}, and the contribution ϕ_{grad} pertaining to the energy of the diffuse interfaces (macroscopic transformation fronts),

$$\phi(\boldsymbol{F}, \bar{\boldsymbol{e}}^{\mathrm{t}}, \eta, \nabla\eta) = \phi_{\mathrm{chem}}(\eta) + \phi_{\mathrm{el}}(\boldsymbol{F}, \bar{\boldsymbol{e}}^{\mathrm{t}}, \eta) + \phi_{\mathrm{int}}(\bar{\boldsymbol{e}}^{\mathrm{t}}, \eta) + \phi_{\mathrm{grad}}(\nabla\eta). \tag{8}$$

Below, a brief description of each contribution is provided.

- The chemical energy ϕ_{chem} is formulated as

$$\phi_{\text{chem}}(\eta) = (1-\eta)\phi_0^{\text{a}} + \eta\phi_0^{\text{m}} = \phi_0^{\text{a}} + \Delta\phi_0\eta, \tag{9}$$

  where ϕ_0^{a} and ϕ_0^{m}, represent, respectively, the reference (stress-free) free energy densities of austenite and martensite phases.

- A neo-Hookean elastic strain energy is adopted in the following form

$$\phi_{\text{el}}(\boldsymbol{F}, \bar{\boldsymbol{e}}^{\text{t}}, \eta) = \frac{1}{2}\mu(\eta)(\text{tr}(\hat{\boldsymbol{b}}^{\text{e}}) - 3) + \frac{1}{4}\kappa(\det(\boldsymbol{b}^{\text{e}}) - 1 - \log(\det(\boldsymbol{b}^{\text{e}}))), \tag{10}$$

  where $\boldsymbol{b}^{\text{e}} = \boldsymbol{F}^{\text{e}}(\boldsymbol{F}^{\text{e}})^{\text{T}}$ is the left Cauchy-Green tensor and $\hat{\boldsymbol{b}}^{\text{e}} = (\det(\boldsymbol{b}^{\text{e}}))^{-1/3}\,\boldsymbol{b}^{\text{e}}$ is the corresponding volume-preserving part. The shear modulus $\mu(\eta)$ is considered to be phase-dependent and is obtained as $1/\mu(\eta) = (1-\eta)/\mu_{\text{a}} + \eta/\mu_{\text{m}}$, with μ_{a} and μ_{m} as the shear moduli of austenite and martensite phases, while the bulk modulus κ is constant.

- The interaction energy ϕ_{int} governs the response of the material within the transformation regime and is simply assumed as a quadratic function of η, i.e.,

$$\phi_{\text{int}}(\bar{\boldsymbol{e}}^{\text{t}}, \eta) = \frac{1}{2}H(\bar{\boldsymbol{e}}^{\text{t}})\eta^2, \tag{11}$$

  where H determines the slope of the response and is assumed to be dependent on the limit transformation strain $\bar{\boldsymbol{e}}^{\text{t}}$ through the following relation,

$$H(\bar{\boldsymbol{e}}^{\text{t}}) = H_{\text{T}} - \frac{(\epsilon_{\text{T}} - \sqrt{2/3}\,\epsilon(\bar{\boldsymbol{e}}^{\text{t}}))(H_{\text{T}} - H_{\text{C}})}{\epsilon_{\text{T}} - \epsilon_{\text{C}}}, \quad \epsilon(\bar{\boldsymbol{e}}^{\text{t}}) = \sqrt{\text{tr}(\bar{\boldsymbol{e}}^{\text{t}})^2}. \tag{12}$$

  Here, H_{T} and H_{C} denote, respectively, the softening modulus in tension and the hardening modulus in compression, $\epsilon_{\text{C}} = \epsilon_{\text{T}}/\alpha$ denotes the maximum transformation strain in uniaxial compression, and $\sqrt{2/3}\,\epsilon(\bar{\boldsymbol{e}}^{\text{t}})$ is the equivalent limit transformation strain.

- Finally, the gradient energy term ϕ_{grad} reads

$$\phi_{\text{grad}}(\nabla\eta) = \frac{1}{2}G\nabla\eta\cdot\nabla\eta, \tag{13}$$

  where $G > 0$ is the corresponding penalization parameter.

It is pertinent to note that the linear dependence between the interaction energy coefficient H and the equivalent limit transformation strain $\sqrt{2/3}\,\epsilon(\bar{\boldsymbol{e}}^{\text{t}})$, as introduced in Eq. (12), is sufficient to adequately calibrate the intrinsic material response in tension, compression and shear (typically, NiTi manifests a softening-type behavior in tension and a hardening-type behavior in compression and shear). Additionally, the quadratic form of the interaction energy ϕ_{int} in Eq. (11) yields a simple trilinear (flag-shaped) intrinsic response. While more sophisticated formulations of the interaction energy could be devised (e.g., Wang et al., 2017) to achieve a more realistic nonlinear intrinsic response (Hallai and Kyriakides, 2013; Alarcon et al., 2017), a deliberate choice is made for a trilinear one. This decision is guided by the recognition that a nonlinear response might also contribute to the striations of the propagating front alongside martensite reorientation, as discussed in more details in Section 4.4. Therefore, with the aim to isolate the effects attributed to martensite reorientation, in line with the primary focus of this paper, a quadratic form of the interaction energy ϕ_{int} is adopted.

2.3. Incremental energy minimization framework

After formulating the Helmholtz free energy function ϕ, a suitable dissipation potential ΔD is defined (to be discussed in the next subsection), thereby establishing all essential components of the incremental energy minimization framework. Subsequently, a global incremental potential Π is constructed from the Helmholtz free energy functional $\Phi = \int_B \phi \, \mathrm{d}V$ and the global dissipation potential $\Delta \mathcal{D} = \int_B \Delta D \, \mathrm{d}V$. The incremental solution is then sought by minimizing Π with respect to the problem unknowns, including the deformation mapping $\boldsymbol{\varphi}$, the limit transformation strain $\bar{\boldsymbol{e}}^{\mathrm{t}}$, and the volume fraction of martensite η. This is expressed as

$$\Pi = \Delta\Phi + \Delta\mathcal{D} + \Delta\Omega \;\rightarrow\; \min_{\boldsymbol{\varphi}, \bar{\boldsymbol{e}}^{\mathrm{t}}, \eta} \tag{14}$$

where $\Delta\Omega$ is the potential energy arising from the external loads. Note that the minimization problem (14) is subject to the constraints specified in Eq. (4). For the general concept, details and applications of the incremental energy minimization principle, the reader is referred to Petryk (2003); Miehe (2011); Stupkiewicz and Petryk (2013); Rezaee-Hajidehi et al. (2020).

2.4. Dissipation potential

The simplest choice for the dissipation potential is the one that considers only the dissipation resulting from the phase transformation, i.e., from the evolution of the martensite volume fraction η. In the time-discrete setting, it takes the form

$$\Delta D(\Delta\eta) = f_{\mathrm{c}} |\Delta\eta|, \tag{15}$$

where $f_{\mathrm{c}} > 0$ is a material parameter (i.e., critical driving force of transformation) that determines the width of the hysteresis loop in the intrinsic response, and $\Delta\eta = \eta - \eta_n$, with η_n as the martensite volume fraction related to the previous time step. This form of dissipation potential can be considered reasonable for applications limited to (predominantly) proportional loading paths (Rezaee-Hajidehi et al., 2020; Rezaee-Hajidehi and Stupkiewicz, 2023).

On the other hand, in cases where the martensite reorientation plays an important role, as for instance under non-proportional loading paths, the model with this simplistic dissipation potential fails to capture appropriately the transformation evolution. This is due to the absence of an energetic cost assigned to the reorientation process, which, in the present formulation, amounts to the lack of dissipation for the evolution of the transformation strain $\boldsymbol{e}^{\mathrm{t}}$. Accordingly, in order to extend the range of applicability of the model, a more generalized dissipation potential ought to be constructed. Two possible choices are explored here, each associated with a specific form of the rate-independent dissipation potential defined for the pair $(\Delta\boldsymbol{e}^{\mathrm{t}}, \Delta\eta)$, where $\Delta\boldsymbol{e}^{\mathrm{t}} = \boldsymbol{e}^{\mathrm{t}} - \boldsymbol{e}^{\mathrm{t}}_{n}$.

The first choice adopts the l_1 norm (also called taxicab norm) of the pair $(\Delta\boldsymbol{e}^{\mathrm{t}}, \Delta\eta)$ and is expressed as,

$$\Delta D(\Delta\boldsymbol{e}^{\mathrm{t}}, \Delta\eta) = \Delta D(\Delta\bar{\boldsymbol{e}}^{\mathrm{t}}, \Delta\eta, \bar{\boldsymbol{e}}^{\mathrm{t}}, \eta) = f_{\mathrm{c}}|\Delta\eta| + \frac{f_{\mathrm{r}}}{\epsilon(\bar{\boldsymbol{e}}^{\mathrm{t}})}\|\Delta\boldsymbol{e}^{\mathrm{t}}\|, \quad \|\Delta\boldsymbol{e}^{\mathrm{t}}\| = \sqrt{\Delta\boldsymbol{e}^{\mathrm{t}} \cdot \Delta\boldsymbol{e}^{\mathrm{t}}}, \tag{16}$$

where f_{r} represents the reorientation dissipation parameter. Notice the normalization of the norm $\|\Delta\boldsymbol{e}^{\mathrm{t}}\|$ by $\epsilon(\bar{\boldsymbol{e}}^{\mathrm{t}})$, cf. Eq. $(12)_2$. This normalization serves dual purposes: first, it aligns the magnitude of f_{r} with that of f_{c}, hence a coherent scaling of dissipation contributions, and second, in line with the definition of the limit transformation strain $\bar{\boldsymbol{e}}^{\mathrm{t}}$, it renders the reorientation dissipation mechanism loading-dependent. Additionally, it is important to note that the term $f_{\mathrm{r}}/\epsilon(\bar{\boldsymbol{e}}^{\mathrm{t}})\|\Delta\boldsymbol{e}^{\mathrm{t}}\|$ brings on additional dissipation associated with the phase transformation. This is because $\boldsymbol{e}^{\mathrm{t}} = \eta\bar{\boldsymbol{e}}^{\mathrm{t}}$, see Eq. (3), and thus any penalization of the evolution of η also penalizes the evolution of $\boldsymbol{e}^{\mathrm{t}}$. Nevertheless, the presence of the transformation-only term $f_{\mathrm{c}}|\Delta\eta|$ is still crucial, as it enables to adequately adjust the contributions arising from the two mechanisms.

The second choice adopts the l_2 norm (Euclidean norm) and takes the form

$$\Delta D(\Delta\boldsymbol{e}^{\mathrm{t}}, \Delta\eta) = \Delta D(\Delta\bar{\boldsymbol{e}}^{\mathrm{t}}, \Delta\eta, \bar{\boldsymbol{e}}^{\mathrm{t}}, \eta) = \sqrt{f_{\mathrm{c}}^2\Delta\eta^2 + \frac{f_{\mathrm{r}}^2}{\epsilon(\bar{\boldsymbol{e}}^{\mathrm{t}})^2}\Delta\boldsymbol{e}^{\mathrm{t}} \cdot \Delta\boldsymbol{e}^{\mathrm{t}}}. \tag{17}$$

In both potentials (16) and (17), upon setting $f_{\mathrm{r}} = 0$, the simplistic case of Eq. (15) is retrieved. Similar forms of dissipation potentials have been devised by Barrera et al. (2014), see also Petrini and Bertini (2020), in the context of pseudoelasticity and functional degradation. Therein, discussions are provided on the physical and mathematical attributes of various dissipation potentials.

As a preface to the finite-element studies presented in Section 4, a material-point analysis is carried out in order to hint on the implications of including the reorientation dissipation in the model. A single material point is subjected to combined non-proportional axial–shear loading within a mixed-type loading control, where the axial strain ε and shear strain γ are prescribed and the axial stress σ and shear stress τ are measured. All the other stress components are constrained to zero. Various axial–shear strain paths are examined, including box-, circular- and butterfly-shaped paths, as illustrated in Fig. 1. To simplify the analysis, a small-strain version of the model is employed, and clearly, the gradient energy term, Eq. (13), is ignored. In this analysis, the constrained minimization problem, cf. Eq. (14), is solved in Mathematica (www.wolfram.com) by using the built-in `FindMinimum` function which relies on the interior-point method. The calculations are done by the models with different forms of dissipation potentials, i.e., Eqs. (15), (16) and (17), which are herein labeled, respectively, as model T, model TR/1 and model TR/2 (T denoting transformation and TR denoting transformation and reorientation). The material parameters are consistent with those adopted in the finite-

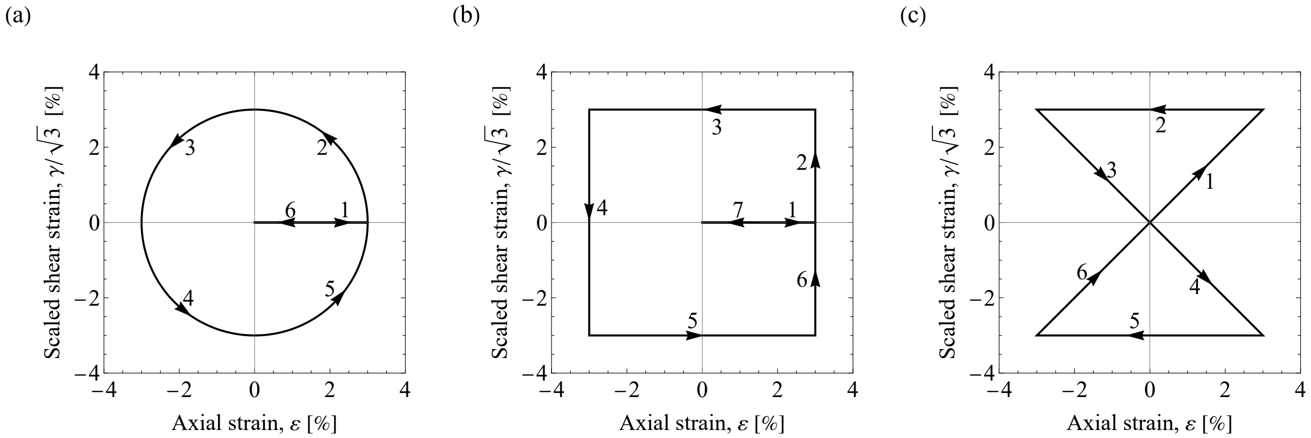

Figure 1: Axial–shear strain paths used in the material-point analysis: (a) circular-shaped, (b) box-shaped, and (c) butterfly-shaped. The maximum axial strain and the maximum (scaled) shear strain in all cases is limited to 3% while the corresponding mean strains are zero.

element study in Section 4.2. The parameters related to dissipation are adopted as: $f_{\rm c} = 6$ MPa for model T, whereas $f_{\rm c} = 3$ MPa and $f_{\rm r} = 3$ MPa for models TR/1 and TR/2.

Fig. 2 collects and compares the responses obtained for different models. A close examination reveals that models incorporating martensite reorientation dissipation, TR/1 and TR/2, are capable of capturing characteristic features overlooked by model T, which align with the experimental observations of Grabe and Bruhns (2009). Particularly noteworthy is the pronounced hysteresis observed in axial and shear responses obtained by TR/1 and TR/2 models within the non-proportional segments of circular- and box-shaped paths, while model T shows considerably smaller hysteresis. Another notable feature pertains to the emergence of positive shear stress at the endpoints of circular- and box-shaped paths (see the proximity of arrow 6 in panel (c) and arrow 7 in panel (f)), which is also missed by model T. At the same time, for the butterfly-shaped path which is characterized by a number of proportional segments, model T presents responses qualitatively similar to those of models TR/1 and TR/2.

Overall, Fig. 2 underlines the importance of martensite reorientation dissipation in capturing a number of intrinsic features at the material-point level. Both l_1 and l_2 norms can be regarded as legitimate choices for the dissipation potential. However, it is important to note that the computational treatment of the l_2-norm dissipation potential could not be done successfully as the resulting finite-element model suffered from severe convergence issues. This, as a result, has prompted the adoption of the l_1-norm dissipation potential for the studies reported in Section 4. Further details on the computational treatment of the model are provided in Section 3.3.

Remark. The dissipation potentials (16) and (17) represent an isotropic dissipation mechanism of martensite reorientation. Both potentials can be readily adapted to an anisotropic case. As an example, the anisotropic version of the l_1-norm dissipation potential is expressed as

$$\Delta D(\Delta \boldsymbol{e}^{\rm t}, \Delta\eta) = \Delta D(\Delta\bar{\boldsymbol{e}}^{\rm t}, \Delta\eta, \bar{\boldsymbol{e}}^{\rm t}, \eta) = f_{\rm c}|\Delta\eta| + \|\Delta\boldsymbol{e}^{\rm t}\|_{\mathbb{D}_{\rm r}}, \qquad (18)$$

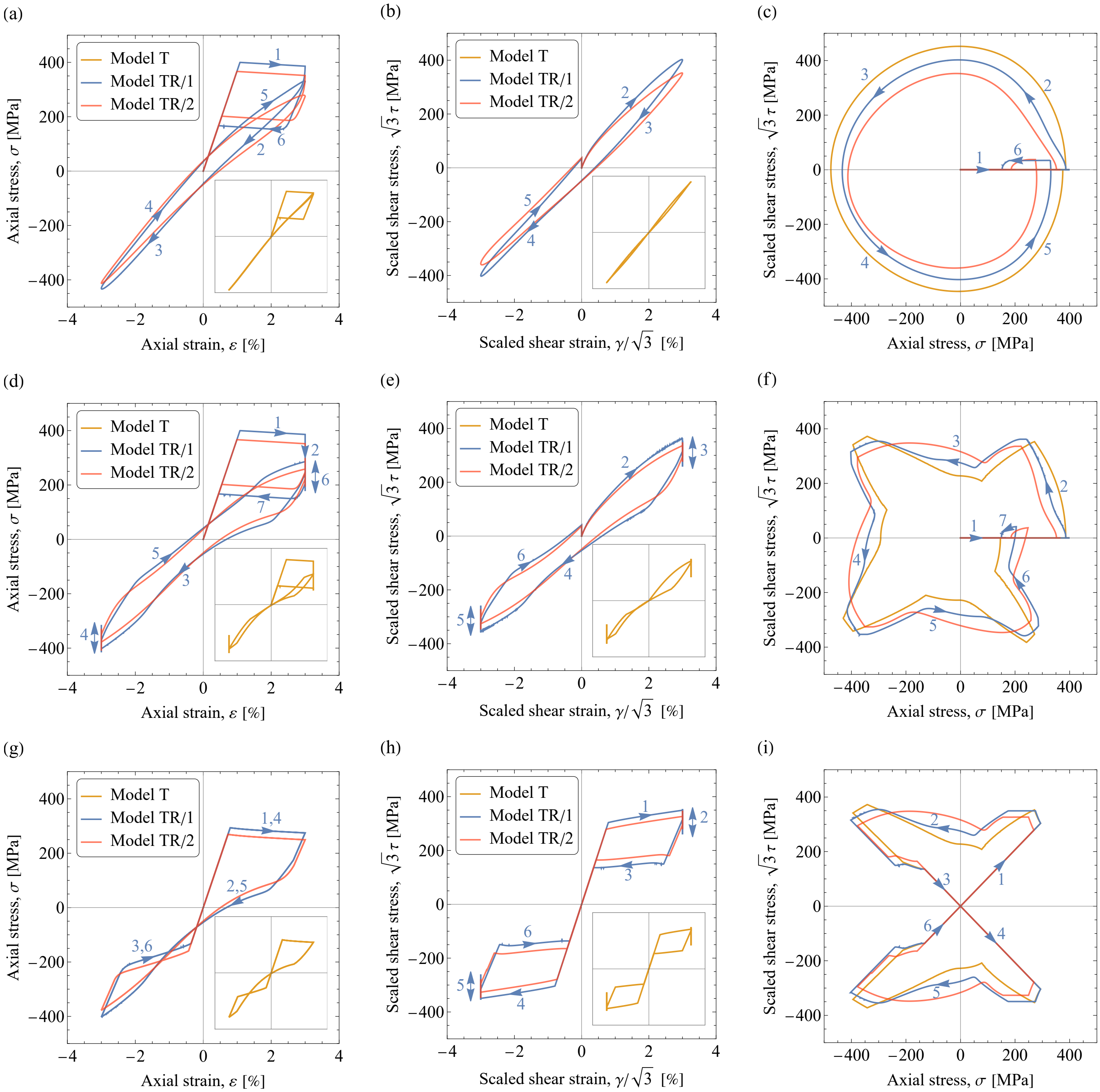

Figure 2: Material-point responses obtained for different dissipation potentials under different axial–shear strain paths: (a,b,c) circular-shaped path, (d,e,f) box-shaped path, and (g,h,i) butterfly-shaped path. Panels (a,d,g) depict the axial stress–axial strain responses, panels (b,e,h) depict the shear stress–shear strain responses, and panels (c,f,i) depict the shear stress–axial stress responses. The superimposed arrows on the plots are solely intended to indicate the trajectories.

where $\|\Delta\boldsymbol{e}^{\mathrm{t}}\|_{\mathbb{D}_{\mathrm{r}}}$ denotes the elliptic norm of the transformation strain increment $\Delta\boldsymbol{e}^{\mathrm{t}}$ relative to $\mathbb{D}_{\mathrm{r}}$, a positive-definite fourth-rank tensor that contains the material parameters associated with reorientation dissipation,

$$\|\Delta\boldsymbol{e}^{\mathrm{t}}\|_{\mathbb{D}_{\mathrm{r}}} = \sqrt{\Delta\boldsymbol{e}^{\mathrm{t}} \cdot \mathbb{D}_{\mathrm{r}}\Delta\boldsymbol{e}^{\mathrm{t}}}. \tag{19}$$

It is worth noting that the finite-element treatment of the anisotropic dissipation potential can be accomplished by extending the augmented Lagrangian function used for the isotropic dissipation (more details in Section 3.3).

3. Finite-element model

In this section, first, the micromorphic regularization and thermomechanical couplings are described, respectively, in Sections 3.1 and 3.2. The computational treatments and implementation of the model are then briefly discussed in Section 3.3.

3.1. Micromorphic regularization

The finite-element implementation of the model hinges on the micromorphic regularization technique (Forest, 2009; Mazière and Forest, 2015). The technique has been successfully employed in our previous studies (Rezaee Hajidehi and Stupkiewicz, 2018; Rezaee-Hajidehi et al., 2020) related to the current context; see Rezaee-Hajidehi and Stupkiewicz (2021a) for the application of the micromorphic technique in phase-field modeling of multi-variant martensitic transformation; see also Yu and Landis (2023) for a more recent application.

The presence of the gradient term ϕ_{grad} in the Helmholtz free energy function ϕ dictates the martensite volume fraction η to be a global degree of freedom. However, the complexities associated with the constitutive equation for η, in particular, the new form of the rate-independent dissipation potential (16), which relies on the coupling between η and the limit transformation strain $\bar{\boldsymbol{e}}^{\mathrm{t}}$, render such a global formulation of η infeasible. Upon resorting to the micromorphic regularization, η can be treated as a local quantity and thus the associated complexities can be efficiently addressed. To this end, a new global degree of freedom $\breve{\eta}$ is introduced and is linked to the martensite volume fraction η via a penalty term ϕ_{pen},

$$\phi_{\mathrm{pen}}(\eta, \breve{\eta}) = \frac{1}{2}\chi(\eta - \breve{\eta})^2, \tag{20}$$

where χ is the corresponding penalty parameter. Clearly, the larger the parameter χ, the better the approximation of η by $\breve{\eta}$. Accordingly, the gradient energy term ϕ_{grad} is rewritten in terms of the gradient of the micromrophic variable $\breve{\eta}$ as $\phi_{\mathrm{grad}} = 1/2G\nabla\breve{\eta} \cdot \nabla\breve{\eta}$. Therefore, the Helmholtz free energy function ϕ takes the following new form

$$\phi(\boldsymbol{F}, \bar{\boldsymbol{e}}^{\mathrm{t}}, \eta, \breve{\eta}, \nabla\breve{\eta}) = \phi_{\mathrm{chem}}(\eta) + \phi_{\mathrm{el}}(\boldsymbol{F}, \bar{\boldsymbol{e}}^{\mathrm{t}}, \eta) + \phi_{\mathrm{int}}(\bar{\boldsymbol{e}}^{\mathrm{t}}, \eta) + \phi_{\mathrm{grad}}(\nabla\breve{\eta}) + \phi_{\mathrm{pen}}(\eta, \breve{\eta}). \tag{21}$$

A new global incremental potential Π is then constructed, cf. Eq. (14), and the minimization problem is solved by minimizing the new incremental potential with respect to the deformation mapping $\boldsymbol{\varphi}$, the limit transformation strain $\bar{\boldsymbol{e}}^{\mathrm{t}}$, the martensite volume fraction η and also the micromorphic variable $\breve{\eta}$. As mentioned above, in light of the micromorphic regularization, η is transformed into a local quantity and its evolution equation, together with that of the limit transformation strain $\bar{\boldsymbol{e}}^{\mathrm{t}}$, is solved locally at each integration point. This translates to the following local minimization problem,

$$\{\bar{\boldsymbol{e}}^{\mathrm{t}}, \eta\} = \arg\min_{\bar{\boldsymbol{e}}^{\mathrm{t}},\eta} \pi(\boldsymbol{F}, \bar{\boldsymbol{e}}^{\mathrm{t}}, \eta, \breve{\eta}, \nabla\breve{\eta}). \tag{22}$$

The local potential π is defined as

$$\pi(\boldsymbol{F}, \bar{\boldsymbol{e}}^{\mathrm{t}}, \eta, \breve{\eta}, \nabla\breve{\eta}) = \phi(\boldsymbol{F}, \bar{\boldsymbol{e}}^{\mathrm{t}}, \eta, \breve{\eta}, \nabla\breve{\eta}) - \phi_n + \Delta D(\Delta\boldsymbol{e}^{\mathrm{t}}, \Delta\eta) + I_{[0,1]}(\eta) + I_{\bar{\mathcal{P}}}(\bar{\boldsymbol{e}}^{\mathrm{t}}), \tag{23}$$

where ϕ_n represents the free energy related to the previous time step, and the indicator functions $I_{[0,1]}$ and $I_{\bar{\mathcal{P}}}$ account for the inequality constraints on the order parameter and the equality constraint of $g(\bar{\boldsymbol{e}}^{\mathrm{t}}) = 0$, respectively,

$$I_{[0,1]}(\eta) = \begin{cases} 0 & \text{if } 0 \leq \eta \leq 1, \\ +\infty & \text{otherwise,} \end{cases} \qquad I_{\bar{\mathcal{P}}}(\bar{\boldsymbol{e}}^{\mathrm{t}}) = \begin{cases} 0 & \text{if } \bar{\boldsymbol{e}}^{\mathrm{t}} \in \bar{\mathcal{P}}, \\ +\infty & \text{otherwise.} \end{cases} \tag{24}$$

On the global level, the minimization is performed with respect to $\boldsymbol{\varphi}$ and $\breve{\eta}$. The corresponding stationarity conditions lead to, respectively, the weak of the mechanical equilibrium (virtual work principle) and the weak form of the averaging Helmholtz-type PDE. Details are omitted for brevity, see Rezaee-Hajidehi et al. (2020).

3.2. Thermomechanical couplings

The thermomechanical extension of the model follows that adopted in the previous versions of the model (Rezaee Hajidehi and Stupkiewicz, 2018; Rezaee-Hajidehi et al., 2020). Specifically, two key thermomechanical coupling effects are incorporated. First, the Clausius–Clapeyron relationship is embedded into the model through establishing a linear dependence between the temperature T and the chemical energy of transformation $\Delta\phi_0$. The chemical energy contribution ϕ_{chem} of the Helmholtz free energy function ϕ is hence reformulated as

$$\phi_{\mathrm{chem}}(\eta, T) = \phi_0^{\mathrm{a}} + \Delta\phi_0(T)\eta, \quad \Delta\phi_0(T) = \Delta s^*(T - T_{\mathrm{t}}), \tag{25}$$

with Δs^* as the entropy difference between pure phases of austenite and martensite and T_{t} as the transformation equilibrium temperature.

Secondly, an internal heat source of transformation/reorientation is introduced in the following (rate) form,

$$\dot{R} = \Delta s^* T\dot{\eta} + f_{\mathrm{c}}|\dot{\eta}| + \frac{f_{\mathrm{r}}}{\epsilon(\bar{\boldsymbol{e}}^{\mathrm{t}})}\|\dot{\boldsymbol{e}}^{\mathrm{t}}\|, \tag{26}$$

where the first term on the right-hand side reflects the latent heat of transformation, while the other two account for the mechanical dissipation and simply correspond to the dissipation potential of the taxicab norm, cf. Eq. (16), expressed here in the rate form. Obviously, the martensite reorientation solely contributes to heat release through mechanical dissipation.

Finally, the heat conduction equation is introduced to the model and is expressed in the following form (Holzapfel, 2006)

$$\varrho_0 c\dot{T} + \nabla \cdot \boldsymbol{Q} = \dot{R}, \quad \boldsymbol{Q} = -K\boldsymbol{C}^{-1}\nabla T, \tag{27}$$

where $\varrho_0 c$ is the specific heat capacity, $\boldsymbol{Q}$ is the nominal heat flux, K is the heat conduction coefficient, and $\boldsymbol{C} = \boldsymbol{F}^{\mathrm{T}}\boldsymbol{F}$ is the right Cauchy-Green strain tensor.

Note that although in all the simulation studies reported in Section 4 relatively low loading rates are applied, hence resulting in minimal temperature effects, the model is deliberately made thermomechanically coupled. This choice is mainly driven by the regularization effects offered by thermomechanical couplings that enhance the robustness of the model even under nearly isothermal conditions.

3.3. Computational treatments and implementation

There are several components of the potential π of the local minimization problem that require careful attention due to their contribution to the non-smoothness of the local problem (23). These include the indicator function $I_{[0,1]}$ representing the inequality constraints $0 \leq \eta \leq 1$, the indicator function $I_{\bar{\mathcal{P}}}$ representing the surface of the limit transformation strain $g(\bar{\boldsymbol{e}}^{\mathrm{t}}) = 0$, and most importantly, the rate-independent dissipation potential ΔD. Recall that ΔD is in the form of the taxicab norm and consists of two terms, the transformation-only term $f_{\mathrm{c}}|\Delta\eta|$ and the term $f_{\mathrm{r}}/\epsilon(\bar{\boldsymbol{e}}^{\mathrm{t}})\|\Delta\boldsymbol{e}^{\mathrm{t}}\|$ that encompasses martensite reorientation dissipation. The non-differentiability arising from each dissipation term must be adequately addressed and the strategy adopted here is based on the augmented Lagrangian method. To this end, two Lagrangian functions are introduced. Firstly, following Stupkiewicz and Petryk (2013), an augmented Lagrangian function l_η is constructed that handles simultaneously the transformation-only part $f_{\mathrm{c}}|\Delta\eta|$ of the dissipation potential and the inequality constraints $0 \leq \eta \leq 1$, via utilization of a single Lagrange multiplier λ_η. The function l_η is formulated as

$$l_\eta(\Delta\eta, \lambda_\eta) = \begin{cases} \lambda_\eta(\Delta\eta - \Delta\eta^-) + \dfrac{\rho_\eta}{2}(\Delta\eta - \Delta\eta^-)^2 - f_{\mathrm{c}}\Delta\eta^- & \text{if } \hat{\lambda}_\eta \leq \rho_\eta\Delta\eta^- - f_{\mathrm{c}}, \\ -\dfrac{1}{2\rho_\eta}\left(\lambda_\eta^2 + 2f_{\mathrm{c}}\hat{\lambda}_\eta + f_{\mathrm{c}}^2\right) & \text{if } \rho_\eta\Delta\eta^- - f_{\mathrm{c}} < \hat{\lambda}_\eta < -f_{\mathrm{c}}, \\ \left(\lambda_\eta + \dfrac{\rho_\eta}{2}\Delta\eta\right)\Delta\eta & \text{if } -f_{\mathrm{c}} \leq \hat{\lambda}_\eta \leq f_{\mathrm{c}}, \\ -\dfrac{1}{2\rho_\eta}\left(\lambda_\eta^2 - 2f_{\mathrm{c}}\hat{\lambda}_\eta + f_{\mathrm{c}}^2\right) & \text{if } f_{\mathrm{c}} < \hat{\lambda}_\eta < \rho_\eta\Delta\eta^+ + f_{\mathrm{c}}, \\ \lambda_\eta(\Delta\eta - \Delta\eta^+) + \dfrac{\rho_\eta}{2}(\Delta\eta - \Delta\eta^+)^2 + f_{\mathrm{c}}\Delta\eta^+ & \text{if } \rho_\eta\Delta\eta^+ + f_{\mathrm{c}} \leq \hat{\lambda}_\eta, \end{cases} \tag{28}$$

where $\hat{\lambda}_\eta = \lambda_\eta + \rho_\eta\Delta\eta$, $\rho_\eta > 0$ is a regularization parameter, and $\Delta\eta^- = -\eta_n \leq 0$ and $\Delta\eta^+ = 1 - \eta_n \geq 0$ are the bounds imposed on the increment $\Delta\eta$.

Secondly, to tackle the non-differentiability of the term $f_{\mathrm{r}}/\epsilon(\bar{\boldsymbol{e}}^{\mathrm{t}})\|\Delta\boldsymbol{e}^{\mathrm{t}}\|$, an augmented Lagrangian function is constructed in the spirit of the frictional contact problem (Alart and Curnier, 1991; Pietrzak and Curnier, 1999). A set of Lagrange multipliers $\boldsymbol{\lambda}_{\mathrm{r}}$, which are conjugate to the transformation strain increment $\Delta\boldsymbol{e}^{\mathrm{t}}$, are introduced. The Lagrangian function l_{r} is then formulated as

$$l_{\mathrm{r}}(\Delta\boldsymbol{e}^{\mathrm{t}},\boldsymbol{\lambda}_{\mathrm{r}})=\begin{cases}\left(\boldsymbol{\lambda}_{\mathrm{r}}+\dfrac{\rho_{\mathrm{r}}}{2}\Delta\boldsymbol{e}^{\mathrm{t}}\right)\cdot\Delta\boldsymbol{e}^{\mathrm{t}} & \text{if } \|\hat{\boldsymbol{\lambda}}_{\mathrm{r}}\|\leq\dfrac{f_{\mathrm{r}}}{\epsilon(\bar{\boldsymbol{e}}^{\mathrm{t}})},\\ -\dfrac{1}{2\rho_{\mathrm{r}}}\left(\|\boldsymbol{\lambda}_{\mathrm{r}}\|^2-\dfrac{2f_{\mathrm{r}}}{\epsilon(\bar{\boldsymbol{e}}^{\mathrm{t}})}\|\hat{\boldsymbol{\lambda}}_{\mathrm{r}}\|+\dfrac{f_{\mathrm{r}}^2}{\epsilon(\bar{\boldsymbol{e}}^{\mathrm{t}})^2}\right) & \text{otherwise,}\end{cases}\tag{29}$$

where $\hat{\boldsymbol{\lambda}}_{\mathrm{r}}=\boldsymbol{\lambda}_{\mathrm{r}}+\rho_{\mathrm{r}}\Delta\boldsymbol{e}^{\mathrm{t}}$ and $\rho_{\mathrm{r}}>0$ is the corresponding regularization parameter. It is worth noting that an anisotropic variant of the friction-type Lagrangian function (29) was previously used in the context of phase-field modeling of multi-variant martensitic transformation for an analogous issue of non-differentiability of rate-independent dissipation effects (Rezaee-Hajidehi and Stupkiewicz, 2021a). For further insights into the formulation procedure, the reader is referred to Appendix A therein.

Lastly, the equality constraint $g(\bar{\boldsymbol{e}}^{\mathrm{t}})$ is enforced by standard penalty regularization method. Consequently, the potential π of the local minimization problem, see Eqs. (22) and (23), is replaced by the following Lagrangian function,

$$L(\boldsymbol{F},\bar{\boldsymbol{e}}^{\mathrm{t}},\eta,\breve{\eta},\nabla\breve{\eta},\boldsymbol{\lambda}_{\mathrm{r}},\lambda_{\eta})=\phi(\boldsymbol{F},\bar{\boldsymbol{e}}^{\mathrm{t}},\eta,\breve{\eta},\nabla\breve{\eta})-\phi_n+l_{\mathrm{r}}(\Delta\boldsymbol{e}^{\mathrm{t}},\boldsymbol{\lambda}_{\mathrm{r}})+l_{\eta}(\Delta\eta,\lambda_{\eta})+\frac{1}{2}\omega g(\bar{\boldsymbol{e}}^{\mathrm{t}})^2,\tag{30}$$

and thereby, the local constrained minimization problem is transformed to the following unconstrained saddle-point problem,

$$\{\bar{\boldsymbol{e}}^{\mathrm{t}},\eta,\boldsymbol{\lambda}_{\mathrm{r}},\lambda_{\eta}\}=\arg\min_{\bar{\boldsymbol{e}}^{\mathrm{t}},\eta}\max_{\boldsymbol{\lambda}_{\mathrm{r}},\lambda_{\eta}}L(\boldsymbol{F},\bar{\boldsymbol{e}}^{\mathrm{t}},\eta,\breve{\eta},\nabla\breve{\eta},\boldsymbol{\lambda}_{\mathrm{r}},\lambda_{\eta}).\tag{31}$$

The complete thermomechanically-coupled problem is structured as a global–local nested iterative–subiterative scheme, where the Newton method is applied to solve the problem at both the local and global levels. The global degrees of freedom include the displacement $\boldsymbol{u}$, the micromorphic variable $\breve{\eta}$ and the temperature T. Within each Newton iteration, the unknowns are solved in a monolithic manner (all at the same time) by a direct linear solver (Intel MKL PARDISO). The finite-element discretization of the global fields is done as follows: 20-noded serendipity hexahedral elements with reduced integration rule are employed for the displacement field $\boldsymbol{u}$, while 8-noded linear hexahedral elements with standard integration rule are employed for the fields of $\breve{\eta}$ and T. The model is translated into a computer code written in Mathematica package AceGen (Korelc, 2009; Korelc and Wriggers, 2016). AceGen is based on automatic differentiation and features code simplification techniques, and thereby, renders the resulting computer code to be optimized and highly efficient. This is crucial for the implementation as it leads to an exact global tangent matrix and guarantees quadratic convergence of the Newton method. The simulations are carried out in the finite-element environment AceFEM.

During the preliminary testing of the finite-element model, it was observed that the model encounters serious convergence issues, particularly in the simulations where strain localization occurs. Upon closer examination, it was discovered that the convergence issues are traced to the poor performance of the friction-type augmented Lagrangian function (29). The issue is then resolved by disuniting the transformation strain $\boldsymbol{e}^{\mathrm{t}} = \eta\bar{\boldsymbol{e}}^{\mathrm{t}}$ that enters the kinematics and the Helmholtz free energy function from the one that enters the friction-type augmented Lagrangian function (29). To achieve this, a new set of local variables are introduced into the model to approximate the transformation strain $\boldsymbol{e}^{\mathrm{t}}$, where the approximation is realized by the penalty regularization method. Subsequently, the original variables of $\boldsymbol{e}^{\mathrm{t}}$ in the Lagrangian function (29) are replaced by the newly introduced variables. This is a simple but potent computational treatment that dramatically improves the performance and robustness of the finite-element model, provided that the related penalty parameter is not too large.

4. Finite-element simulations

Three distinct numerical studies are carried out to assess the range of applicability of the model and showcase its ability in capturing various experimentally-observed features. Each numerical study corresponds to a particular experimental scenario and in each case comparisons with the experimental results are made to validate the obtained results. The first study concerns a NiTi tube specimen subjected to combined non-proportional tension–torsion loading. This study refers to the experiment of McNaney et al. (2003). The aim of the study is to demonstrate the immediate implications of incorporating martensite reorientation dissipation into the model. In the second study, with reference to the experiment of Bechle and Kyriakides (2014), a NiTi tube under pure bending is analyzed. This study highlights the role of martensite reorientation dissipation as a crucial modeling asset that enables the successful simulation of this specific scenario. The third numerical study explores the striations of the propagating fronts, a subtle characteristic of the martensitic transformation pattern that, despite its emergence, is often overlooked in the experiments and modeling studies. Here, the importance of martensite reorientation dissipation in capturing and controlling the striations is underlined. While striations have been noted in several experiments, the more recent experimental study by Shariat et al. (2022) serves as a reference for the current investigation.

4.1. Choice of the model parameters

Table 1 lists the model parameters adopted in the numerical studies. There exist certain parameters that remain consistent across all the three studies and their values are sourced from the existing literature data. These include the bulk modulus $\kappa = 130$ GPa, the specific entropy difference $\Delta s^* = 0.24$ MPa/K, and the parameters that govern the heat flow: the heat conductivity coefficient $K = 18$ W/(m K) and the specific heat capacity $\varrho_0 c = 2.86$ MJ/(m^{3}K). At the same time, the material parameters that characterize the intrinsic mechanical responses are calibrated based on the structural response of the related experiment. This calibration involves adjusting the trilinear (softening-type) response in tension to align its Maxwell construction within the forward and reverse transformation with the stress plateau observed in the experiment. As a result of this, the austenite and martensite shear moduli μ_{a} and μ_{m}, the transformation equilibrium temperature T_{t}, the dissipation parameter f_{c}, the tensile transformation strain ϵ_{T}, and the softening modulus H_{T} are selected. It is worthwhile

Table 1: Parameters adopted in the numerical studies.

Parameter		Unit	Value (study 1)	Value (study 2)	Value (study 3)
Δs^*	Specific entropy difference	MPa/K	0.24	0.24	0.24
κ	Bulk modulus	GPa	130	130	130
μ_a	Shear modulus for austenite	GPa	12.7	21.1	10.3
μ_m	Shear modulus for martensite	GPa	8.6	9.8	6.8
T_t	Transformation equilibrium temperature	K	236	214	234
f_c	Dissipation parameter (reference value)	MPa	3	3.5	3
f_r	Dissipation parameter (reference value)	MPa	3	3.5	3
ϵ_T	Maximum transformation strain in tension	[-]	4.8%	5.3%	5.2%
H_T	Softening modulus in tension	MPa	-2	-8	-5
H_C	Hardening modulus in compression	MPa	8	8	8
α	Tension–compression asymmetry ratio	[-]	1.2	1.4	1.4
β	Transverse isotropy parameter*	[-]	1.0	1.0	1.0
G	Gradient energy parameter	Pa mm^2	50	350	10^4
χ	Micromorphic penalty parameter	MPa	200	850	500
K	Heat conductivity coefficient	W/(m K)	18	18	18
$\varrho_0 c$	Specific heat capacity	MJ/(m^{3}K)	2.86	2.86	2.86

* The axis of transverse isotropy alignes with the longitudinal axis of the specimen.

to acknowledge the inherent ambiguity (and thus freedom) in the selection of the softening modulus H_T, as it cannot be directly inferred from the experimental plateau-type response. This delicate issue is discussed in more details in Rezaee-Hajidehi and Stupkiewicz (2023). Next, the intrinsic response in compression and/or shear is refined by calibrating the tension–compression asymmetry parameter α, the transverse isotropy parameter β, and the hardening modulus H_C. This refinement is particularly pertinent to numerical studies 1 and 2, which involve combined tension–torsion loading and pure bending, respectively, with the corresponding parameters determined based on the structural response under pure torsion and uniaxial compression. To illustrate the outcome of the parameter identification process, Fig. 3 depicts the tensile and compressive intrinsic responses related to numerical study 2.

One important point to highlight regards the selection of the dissipation parameter f_r. In the present formulation, the dissipation mechanisms of phase transformation and reorientation cannot be fully decoupled, cf. Eq. (16). This is a limiting factor that does not allow an accurate determination of the reorientation-only hysteresis magnitude in the model. Given that, the admissible range for f_r is selected with reference to the mechanical responses of macro-scale experiments of pseudoelasticity (e.g., Grabe and Bruhns, 2009; McNaney et al., 2003). From the outcome of the preliminary analysis it follows that f_r should be of the same order of magnitude as that of the transformation-only dissipation parameter f_c. Therefore, in all the three numerical studies reported below the reference value for f_r is set equal to f_c. Note that, a major part of the investigation in each study is dedicated to the parametric study examining the impact of the dissipation parameters f_c and f_r. It is important to point out that in view of the construction of the dissipation potential (16), as long as the sum of f_c and f_r remains fixed, any alternation in their values will not affect the dissipation associated with phase transformation in simple proportional loading paths.

It remains to properly choose the gradient energy parameter G and the micromorphic penalty parameter χ. These parameters are identified by means of the analytical solution

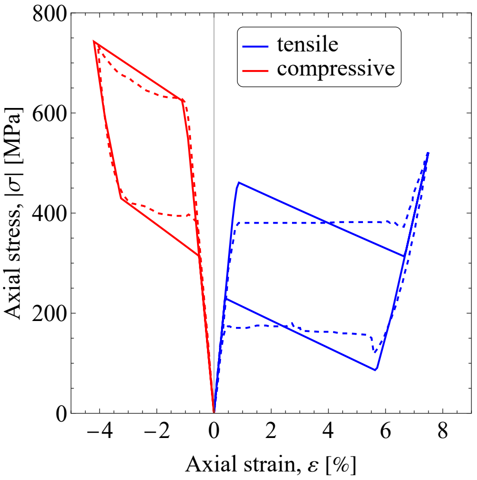

Figure 3: The intrinsic response in tension and compression calibrated for the numerical example of NiTi tube under pure bending (Section 4.3). The dashed curves represent the structural responses obtained in the experiment of Bechle and Kyriakides (2014) at 23°.

of the corresponding 1D model (Rezaee Hajidehi and Stupkiewicz, 2018). Concerning the gradient energy parameter G, a suitable value for the thickness of the theoretical interface, λ, is assumed first. The parameter G is then calculated based on the analytical relation $G=-H_{\mathrm{T}}\lambda^2/\pi^2$. It is necessary to highlight that in 3D simulations, beyond the regularization provided by the gradient term in the free energy, additional regularization arises from the 3D geometry of the problem, specifically, from the 3D deformation state of the specimen (He and Sun, 2009; Rezaee-Hajidehi et al., 2020). Notably, as discussed in our previous study (Rezaee-Hajidehi et al., 2020), the larger the specimen's thickness the larger the 3D effects. This implies that the 'actual' thickness of the austenite–martensite diffuse interfaces obtained in the simulations is larger compared to the theoretical thickness given by the gradient-enhanced model. In addition, our experience with the simulation of thick-walled NiTi tubes indicates that opting for a relatively low value of G is necessary to preserve the subtle morphological pattern of the transformation front, while still providing adequate regularization effects.

Based on the above discussion, a small value of λ is employed in numerical studies 1 and 2, hence a small value of G. At the same time, in numerical study 3 which involves straight NiTi specimens, an interface thickness equal to the finite-element size is considered, $\lambda=0.14$ mm, which results in $G=10^4$ Pa mm^2. Note also that the finite-element mesh adopted to discretize the geometries is too coarse to exclude all the possible numerical artifacts that may arise. However, as confirmed by the results of our auxiliary simulations, the artifacts are not severe enough to impose qualitative influences. As a side remark, it is worth noting that in 2D problems, regularization is solely governed by the gradient energy. Therefore, it is crucial to adjust carefully the element size in relation to the theoretical interface thickness to ensure a proper resolution of the interfaces (Yu and Landis, 2023).

Finally, the rationale behind the choice of the micromorphic parameter χ is that it must be adequately large to ensure a close correlation between the local variable η and the global unknown $\breve{\eta}$ without compromising the computational performance.

4.2. Numerical study 1: NiTi tube under non-proportional tension–torsion

An hourglass-shaped thin-walled NiTi tube of the total length of $L_0 = 75$ mm was used in the experiment of McNaney et al. (2003). The tube had an inner diameter of 3.9 mm throughout the entire length, a wall thickness of 0.2 mm along the 25 mm central segment, and a wall thickness of 0.37 mm elsewhere. The tube was subjected to both proportional and non-proportional tension–torsion in a displacement-control loading configuration with various combinations of maximum axial and shear strains. The experiments were conducted at an ambient temperature of 22° and the applied strain rate corresponded to nearly isothermal conditions. The same setup is mimicked in the present numerical study. To comply with the aim of the study, only non-proportional loading is considered. Representative torsion-then-tension and tension-then-torsion paths are examined, where the prescribed shear strain γ is limited to 4% while the prescribed axial strain ε takes two maximum values: 3% and 6%. The unloading phase in each path is applied in a reverse order as that of loading. A reasonably fine mesh density is used. The tube is discretized using elements with an in-plane size of 0.15 mm. To prevent overly expensive computations, the mesh is coarsened outside the 25 mm central segment, and only one element is used through the thickness. Note that the reference values of the dissipation parameters for this analysis are $f_{\mathrm{c}} = f_{\mathrm{r}} = 3$ MPa.

Following the convention of McNaney et al. (2003), the mechanical responses are presented here in terms of the equivalent stress σ_{eq} and equivalent strain $\varepsilon_{\mathrm{eq}}$, which are defined as

$$\sigma_{\mathrm{eq}} = \sqrt{\sigma^2 + 3\tau^2}, \quad \varepsilon_{\mathrm{eq}} = \sqrt{\varepsilon^2 + \gamma^2/3}, \tag{32}$$

where σ and τ denote, respectively, the nominal axial stress and the nominal shear stress.

An important observation in the torsion-then-tension simulations with a maximum axial strain of 6% was the occurrence of the so-called helical buckling during unloading, which has not been reported by McNaney et al. (2003). To avoid buckling, the thickness of the tube in the 25 mm central segment has been increased to 0.25 mm for this particular loading path. The case demonstrating the helical buckling is thus removed from the main analysis in this section and the corresponding results are deferred to Appendix A.

Fig. 4 illustrates the mechanical responses predicted by the model for torsion-then-tension loading paths and compares them with those from the experiment. For a comprehensive comparison, the responses obtained without the reorientation dissipation are also included in the figure, as indicated by dashed curves. It is evident at the first glance that the incorporation of reorientation dissipation gives rise to admirable results. The mechanical response displays two hallmarks: one during loading when the maximum shear strain of 4% is attained and the axial strain starts to apply, and the other during unloading when the axial strain decreases towards zero. The significant stress variations linked to these two characteristic instants have been effectively captured by the model, albeit with some quantitative discrepancies, especially related to the underestimation of the stress rise during unloading. From the comparison in Fig. 4 it is clear that in the absence of reorientation dissipation the model fails to capture properly the two hallmarks of the mechanical response. On the other hand, in tension-then-torsion loading paths, as depicted in Fig. 5, the simulation results with and without the

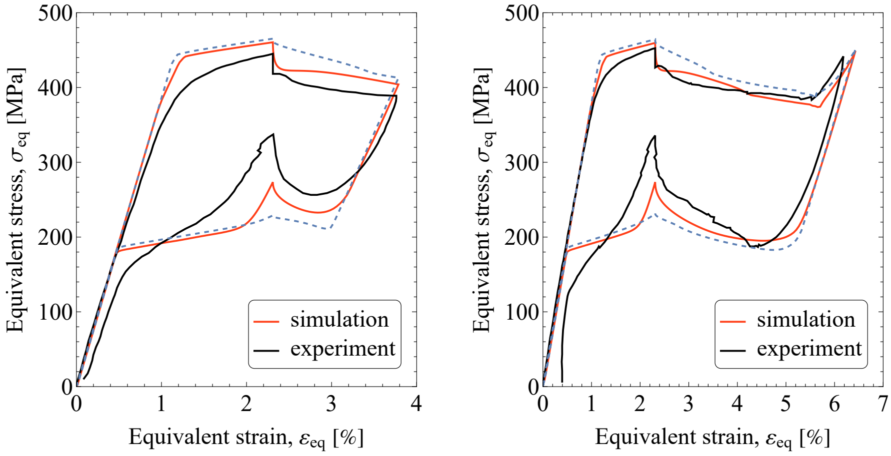
(a) torsion (4%) ⟶ tension (3%)

(b) torsion (4%) ⟶ tension (6%)

Figure 4: NiTi tube under torsion-then-tension: the predicted equivalent stress–equivalent strain response compared with that from the experiment of McNaney et al. (2003). The blue dashed lines represent the simulation results with no dissipation due to reorientation, i.e., $f_{\text{c}} = 6$ MPa and $f_{\text{r}} = 0$.

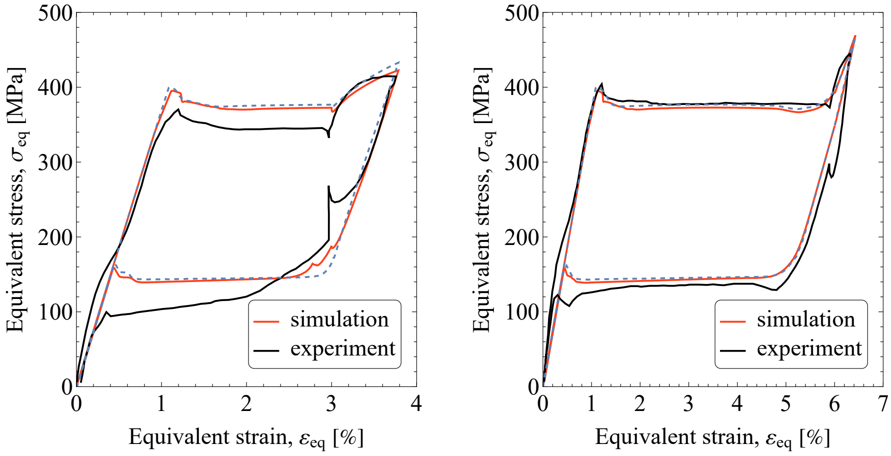
(a) tension (3%) ⟶ torsion (4%)

(b) tension (6%) ⟶ torsion (4%)

Figure 5: NiTi tube under tension-then-torsion: the predicted equivalent stress–equivalent strain response compared with that from the experiment of McNaney et al. (2003). The blue dashed lines represent the simulation results with no dissipation due to reorientation, i.e., $f_{\text{c}} = 6$ MPa and $f_{\text{r}} = 0$.

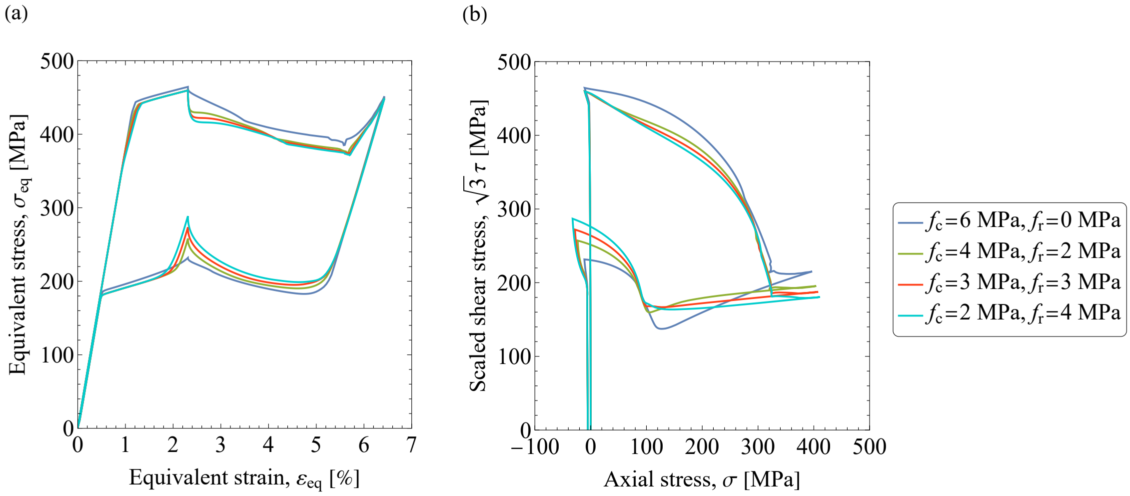

Figure 6: NiTi tube under torsion (4%) followed by tension (6%): the effect of the dissipation parameters f_{c} and f_{r} on (a) the equivalent stress–equivalent strain response and (b) shear stress–axial stress response.

reorientation dissipation exhibit great similarity. Minor differences can be observed between the responses in the case with 3% of axial strain. In particular, sudden stress changes at the beginning of reverse transformation during unloading have been reproduced with reorientation dissipation, which are, however, visibly less significant compared to the stress drop seen in the experiment. At the same time, almost identical responses in the case with 6% of axial strain are predicted. In this case, the small hallmark at the beginning of unloading is totally missed in the simulations.

The observations from Fig. 5 are supplemented by two important remarks. Firstly, auxiliary analysis (results not shown here) has revealed that the softening modulus H_{T} visibly influences the magnitude of the stress variations. As discussed previously, there exists a degree of flexibility in adopting the value of H_{T} and its definitive determination cannot be based solely on the structural response in the experiment. Secondly, in the case with an allowable axial strain of 6%, nearly full transformation is achieved at the onset of applying the shear strain, which potentially explains the absence of stress variation in the predicted response during unloading.

Next, the impact of the dissipation parameters f_{c} and f_{r} on the simulation results is explored. The loading path chosen for this investigation is torsion-then-tension with a maximum axial strain of 6%. The reason for this choice is twofold. Firstly, unlike the case with a maximum axial strain of 3%, this case presents a localized phase transformation, which is also intriguing to examine. Secondly, as follows from Figs. 4 and 5, the role of the reorientation dissipation mechanism in torsion-then-tension scenario is more important than in tension-then-torsion. Fig. 6(a) shows the mechanical responses in terms of the equivalent stress–equivalent strain for various combinations of f_{c} and f_{r}. A systematic tendency is obviously found: the larger the parameter f_{r}, the more pronounced the characteristic stress variations. To enrich the analysis, the mechanical responses in terms of the shear stress–axial stress are also compared (Fig. 6(b)), highlighting the impact of reorientation dissipation from a different viewpoint.

The discussion concludes with a comparison of the transformation patterns for the cases

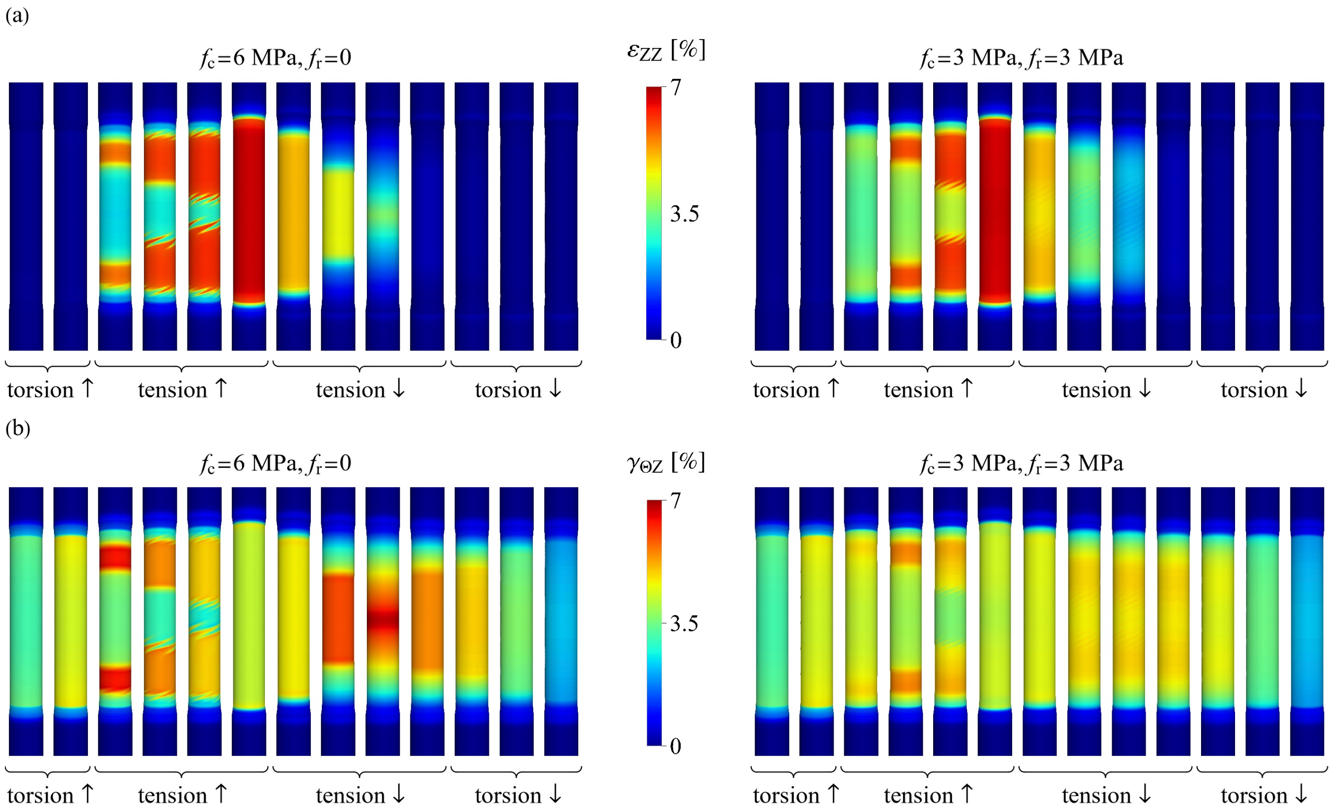

Figure 7: NiTi tube under torsion (4%) followed by tension (6%): snapshots of the axial strain field ε_{ZZ} (a) and shear strain field $\gamma_{\Theta Z}$ (b) for the simulations without and with the dissipation due to martensite reorientation, respectively, with $f_c = 6$ MPa and $f_r = 0$ (snapshots on the left) and $f_c = 3$ MPa and $f_r = 3$ MPa (snapshots on the right).

with and without the reorientation dissipation, as shown in Fig. 7. Transformation patterns are represented by the components of the Green–Lagrange finite–strain measure (a convention that is consistently used in the subsequent studies). Noticeable differences are discernible, particularly concerning the level of axial and shear strains during the transformation, as well as the detailed morphology of the transformation front in propagation. Since no information on the transformation pattern from the experiment of McNaney et al. (2003) is available, the validity of the results in Fig. 7 remains elusive.

4.3. Numerical study 2: NiTi tube under bending

Pseudoelastic NiTi tubes exhibit an attractive phase transformation pattern when subjected to bending. As documented by Bechle and Kyriakides (2014), diamond-shaped martensite regions with high strain/curvature localization emerge on the tensioned side of the tube, which gradually spread and dominate over the whole length. Conversely, the transformation on the compressed side of the tube is uniform, albeit not entirely so due to the high strain/curvature localization effects on the tensioned side. The transformation is accompanied by a plateau-type moment–curvature response that resembles the typical response of NiTi specimens under tension. The intricate behavior of NiTi tube under bending is attributed to arise from the combined effects of tube's circular geometry and the tension–compression asymmetry inherent in the material (Watkins et al., 2018).

The focus of this section is the analysis of a NiTi tube under pure bending. The study draws upon the experiment of Bechle and Kyriakides (2014) whose modeling was later performed by Jiang et al. (2017a). It is important to stress here that the success of such a modeling endeavor hinges on the inclusion of martensite reorientation dissipation. Without it, the model fails immediately at the onset of localized transformation. This failure is believed to result from the uncontrolled growth of the transformation strain within the localization zone, leading to a form of local buckling in the tube that disrupts the simulation. However, when the reorientation dissipation comes into play, the transformation strain evolves in a physically reasonable manner, and this hinders the occurrence of buckling. In this section, the simulation results based on the reference values of the dissipation parameters $f_{\mathrm{c}} = f_{\mathrm{r}} =$ 3.5 MPa are investigated first, with the aim to demonstrate the capability of the model in capturing essential features. Subsequently, the impact of the dissipation parameters on the simulation results is examined.

Adhering to the specifications provided by Bechle and Kyriakides (2014), the tube under study possesses an outer diameter of 5.11 mm, a wall thickness of 0.625 mm, and a length of $2L_0 = 76.7$ mm. In the experimental setup, the tube underwent isothermal bending using a custom-built device designed for pure bending. To mimic pure bending, idealized boundary conditions are enforced here. Following Hallai and Kyriakides (2011), the end sections are assumed to remain plane while being free to ovalize. This constraint is expressed as

$$\tan\theta_{\mathrm{end}} = \frac{x_{\mathrm{ref}} - x_i}{z_{\mathrm{ref}} - z_i}, \tag{33}$$

where x_i and z_i denote the coordinates of the nodes located on the end sections, x_{ref} and z_{ref} the coordinates of the corresponding reference node, and θ_{end} the prescribed rotation angle.

By leveraging the symmetry about the plane of bending, only one half of the cross section is simulated, with appropriate symmetry conditions enforced at the cut surface. The symmetry about the mid-span can also be taken advantage of, so that only one quarter of the complete geometry is simulated. To illustrate the significance of this symmetry consideration, the main simulation is performed twice, once with the symmetry disregarded and once with the symmetry exploited. These cases are referred to, respectively, as ‘full tube’ and ‘half tube’ in the sequel. A uniform finite-element mesh is adopted in the simulations with equiaxed elements of the size 0.21 mm, i.e., 3 elements are used through the thickness. Auxiliary simulations have confirmed the adequacy of this mesh density, as a finer mesh density did not lead to any appreciable improvement in the results. Note that to initiate the transformation localization consistently in all the simulations, a geometrical imperfection is introduced on the top edge close to the end section.

Let’s first delve into the simulation results of the full tube and compare them with the experimental data. Figs. 8(a) and 9 depict the predicted and experimental bending moment–end rotation responses and phase transformation evolutions, respectively. The predicted mechanical response is normalized using the same variables $M_0 = 4790$ N mm and $\kappa_0 = 0.0032$ mm^{-1}

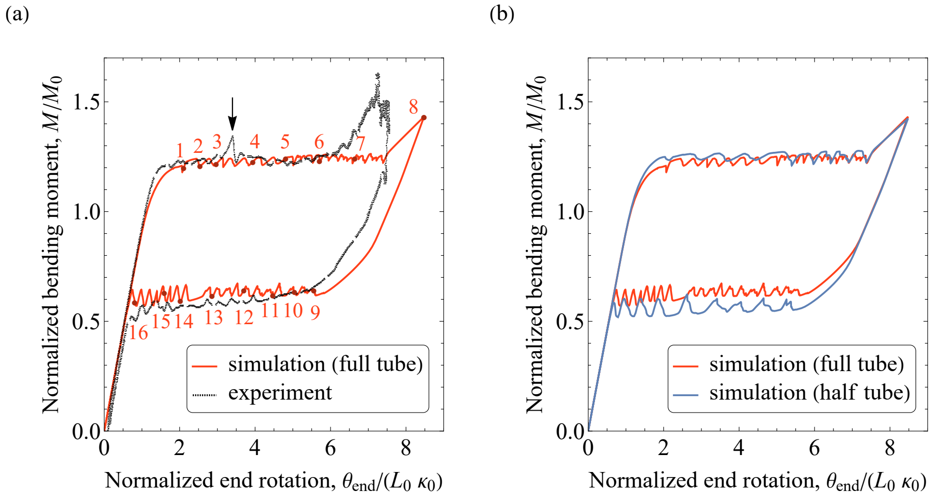

Figure 8: NiTi tube under bending: (a) comparison between the predicted bending moment–end rotation response with that from the experiment of Bechle and Kyriakides (2014) and (b) comparison between the bending moment–end rotation responses obtained for the simulations with full tube and half tube.

as those employed in the experiment, see Table 1 of Bechle and Kyriakides (2014). Recall that the axial component of the Green–Lagrange strain measure is used to represent the transformation pattern. To accentuate the similarities between the transformation patterns, the same color contour as that in the experiment is used. Numerous similarities become immediately apparent. Firstly, the upper and lower moment plateaus are well captured by the model. Although, on average, the lower plateau exhibits a slightly higher level of moment than that in the experiment, overall, the agreement is good. Unlike the typical transformation evolution observed in tension, the transformation under bending does not feature a propagating front. Instead, individual martensite domains nucleate continuously and turn into diamond-shaped pockets. A similar pattern is observed during unloading. The raggedness of the moment plateaus is indeed linked to this continuous domain nucleation and is qualitatively comparable with that reproduced by the model. A notable difference in the mechanical responses concerns the extent of the upper moment plateau, which is larger in the predicted response. This observation was also made in the modeling study of Jiang et al. (2017a). One possible reason for this inconsistency is related to the extent of the transformation regime in the material response under uniaxial compression. A close examination of Fig. 3 reveals that the structural response in the experiment represents a nearly complete transformation under compression, as the corresponding response is about to enter the stiff branch of saturated martensite (Fig. 5 in Bechle and Kyriakides (2014) clearly shows this nearly complete transformation). At the same time, in the calibrated intrinsic response, the material still remains within an incomplete transformation state under the maximum applied strain, with a martensite volume fraction of about $\eta = 0.6$. This is in fact due to the limitation of the model that does not allow a full quantitative calibration of the intrinsic responses in both tension and compression, see the related discussion in Rezaee-Hajidehi and Stupkiewicz (2023). Another noticeable and delicate difference in the mechanical responses is that the experimental curve shows a moment increase

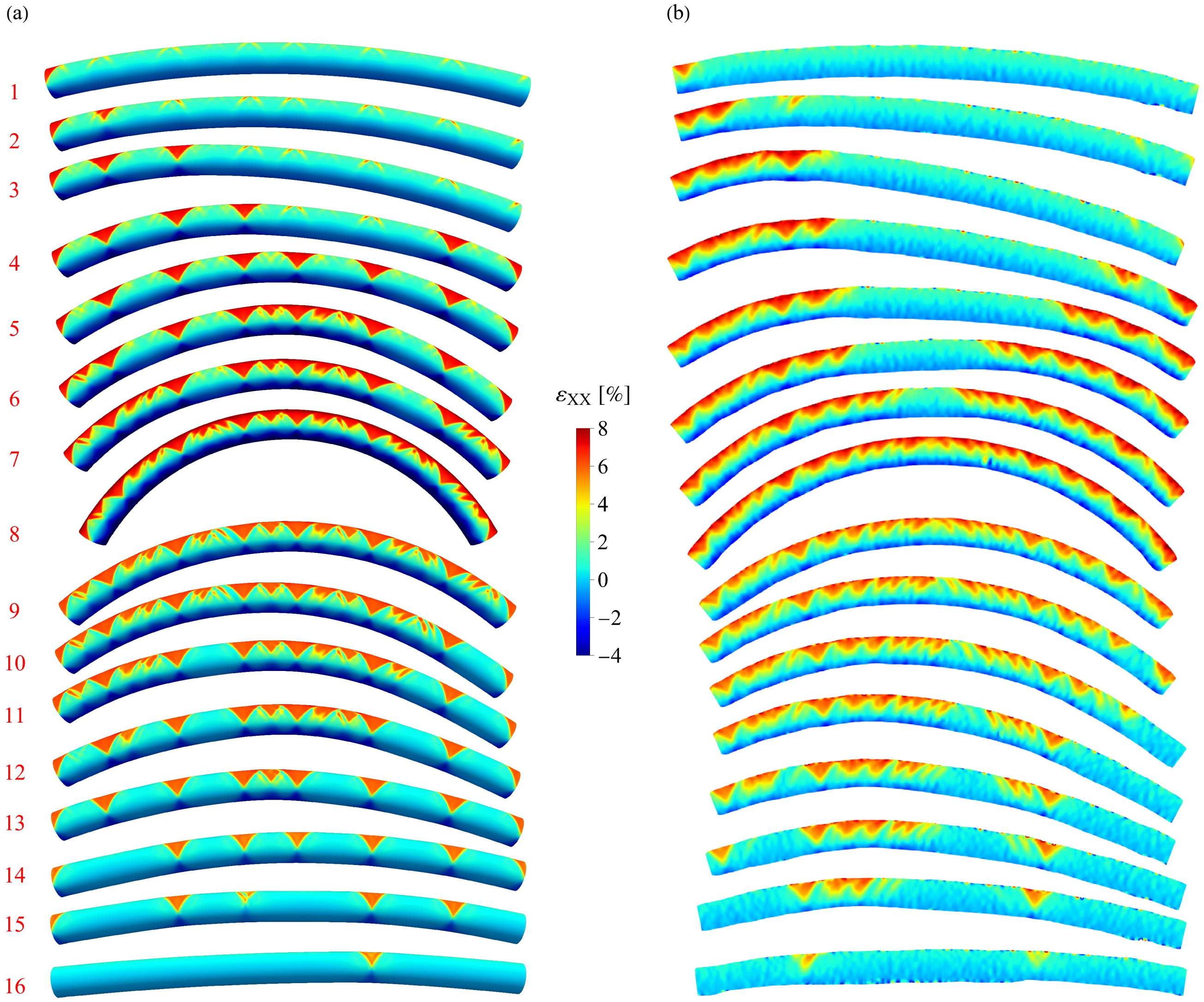

Figure 9: NiTi tube under bending: comparison between (a) the predicted transformation evolution and (b) the transformation evolution observed in the experiment of Bechle and Kyriakides (2014) (reproduced with permission from Elsevier). The experimental snapshots are taken from the paper of Jiang et al. (2017a). The numbers marking the simulation snapshots correspond to those indicated on the mechanical response in Fig. 8(a).

between instants 3 and 4 (as indicated by the arrow in Fig. 8(a)). This is likely related to the saturation of the transformation in the high-curvature region of the tube, which is followed by an elastic deformation throughout the tube. As transformation nucleates in the other end of the tube, the moment drops and continues along the original plateau. This feature has not been captured in the model prediction.

Regarding the transformation evolution, the resemblance to the experiment is striking, with many essential features being well captured. One particularly interesting feature is the co-existence of high-curvature and low-curvature regions, clearly evident in the deformed tube configuration, see e.g., snapshots 3 or 11 in Fig. 9. This aspect is further discussed later on. On the other hand, one notable disparity lies in the manner in which the martensite domains spread throughout the entire tube during loading. In the simulation, the transformation proceeds via the formation of diamond-shaped pockets of martensite that are visibly separated from each other. The spaces between the pockets are then filled by smaller and more randomly oriented domains. In the experiment, however, such clear spacing between the individual pockets is not as prominent.

The assumption of symmetry about the mid-span is a common practice in modeling tube specimens under bending (Hallai and Kyriakides, 2011; Jiang et al., 2017a; Kazinakis et al., 2021; Frost et al., 2021). Here, as a side analysis, the implications of enforcing this symmetry on the results are explored. Figs. 8(b) and 10 compare the simulation results between the full tube and half tube configurations, with the latter implementing this symmetry consideration. Fig. 8(b) reveals two marked differences in the mechanical response. The major one concerns the value of the transformation-onset moment during unloading and the level of ensuing moment plateau, which are lower in the half tube simulation. Additionally, the number of oscillations within the ragged plateaus in the half tube simulation is visibly lower than that in the full tube. This is mostly the consequence of halving the tube in length, and hence reducing the number of domain nucleations. The comparison of the transformation evolutions in Fig. 10 suggests that the prediction made by half tube configuration is reasonably accurate, as the main features are correctly captured. However, one point that deserves further attention regards the distribution of curvature along the tube's length. In the full tube simulation, the division of the tube into high-curvature and low-curvature zones is evident. Such a division is not possible in the half tube configuration, as the tube lacks sufficient freedom to accommodate it. This aspect is reflected in the distribution of slope θ along the tube's length in Fig. 11 (note that the distribution of curvature can be readily envisioned from the distribution of slope). The top fiber of the tube, which is under maximum tension, is chosen for this analysis. Setting aside the local slope variations, it can be seen that as the loading increases/decreases the slope in the half tube configuration increases/decreases in a somewhat more uniform fashion compared to the full tube. The co-existence of high- and low-curvature zones in the full tube can be conceived from the overall trend of the graphs as well as the asymmetry of the graphs about the centerline, see the magnified views in Fig. 11(a,b).

Finally, the impact of the dissipation parameters f_c and f_r on the simulation results is discussed. In view of the high computational cost associated with full tube simulation, the

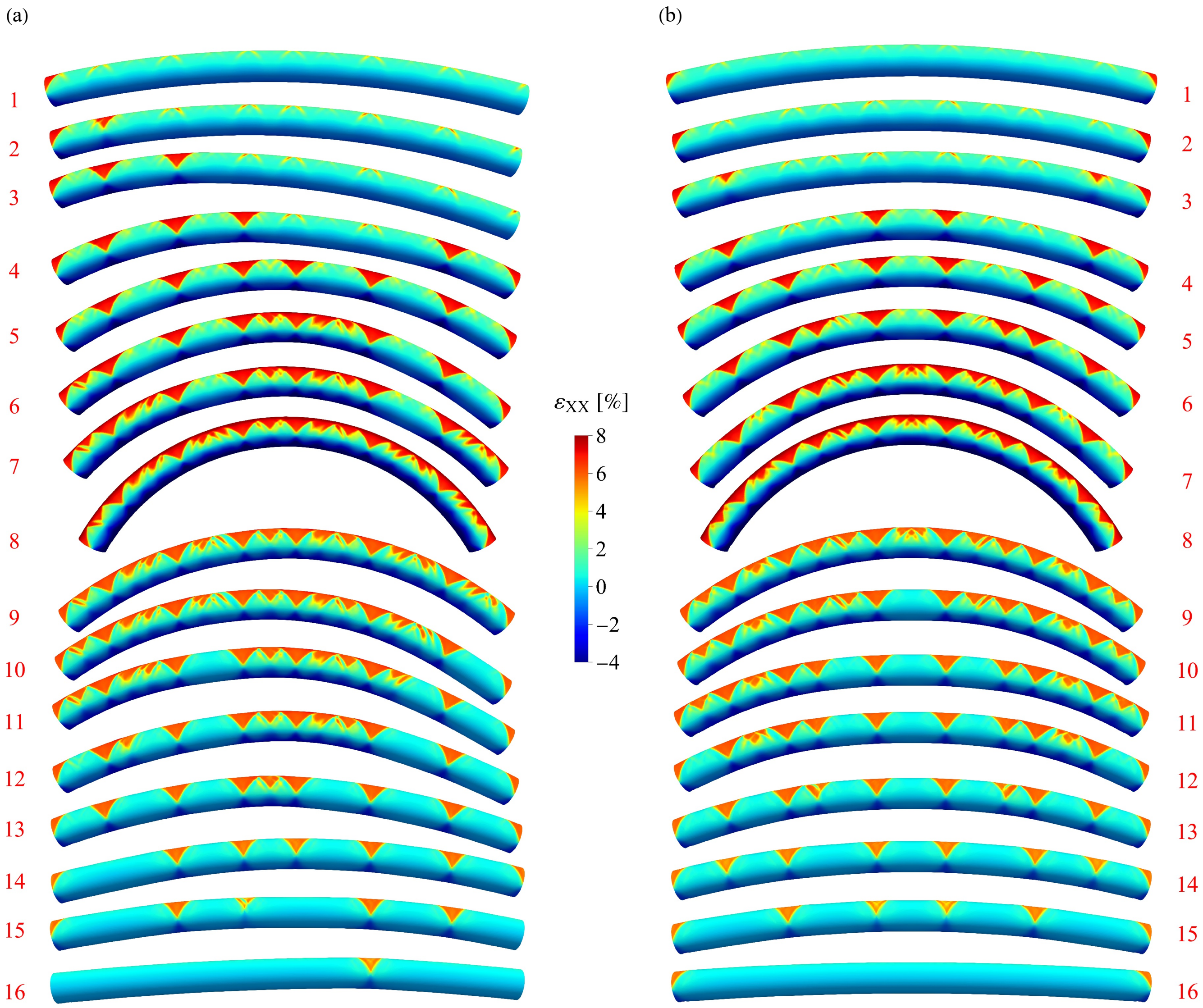

Figure 10: NiTi tube under bending: comparison between the transformation evolutions in the simulations with (a) full tube and (b) half tube. For the ease of comparison, the half tube is reflected along the plane of symmetry (mid-span) and is shown as full. The snapshots correspond to nearly the same prescribed angle θ_{end}.

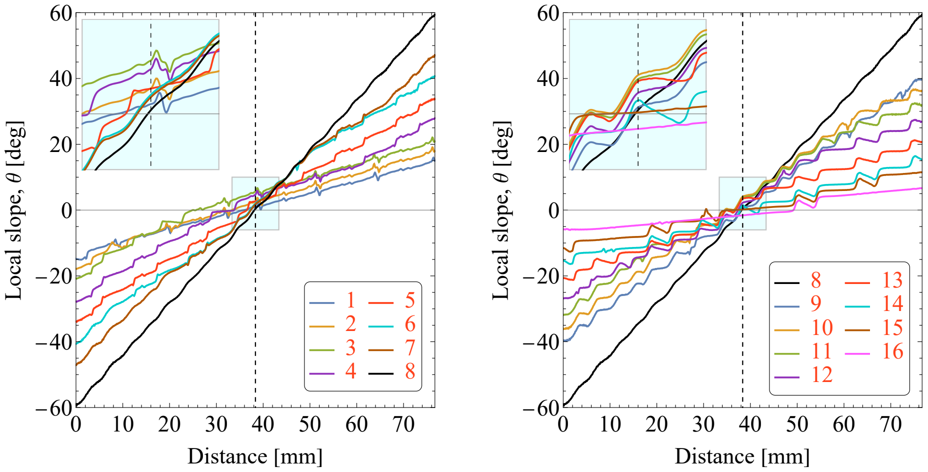
(a) full tube (loading)

(b) full tube (unloading)

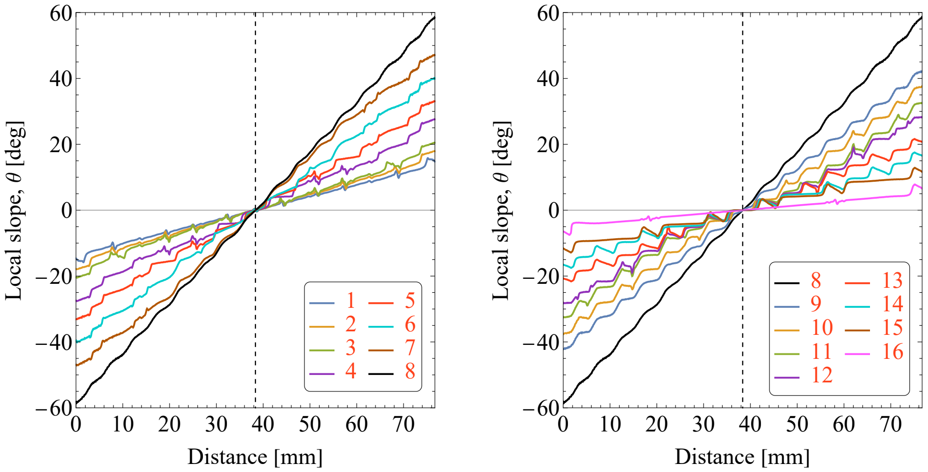
(c) half tube (loading)

(d) half tube (unloading)

Figure 11: NiTi tube under bending: distribution of the slope along the tube at various stages of loading and unloading for (a,b) full tube and (c,d) half tube. The numbers in the legends correspond to the deformation stages shown in Fig. 10. For the ease of comparison, the plots related to half tube are reflected along the plane of symmetry (mid-span) and are shown as full. The vertical dashed line indicates the mid-span of the undeformed tube.

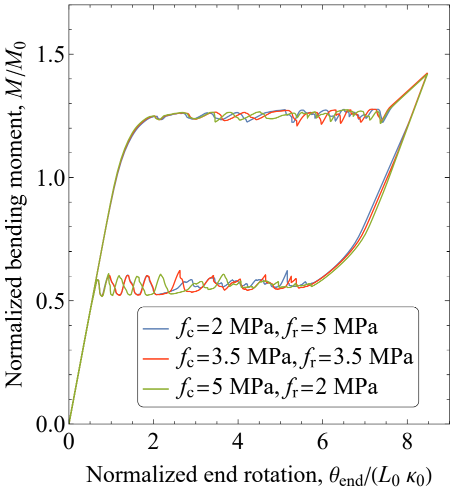

Figure 12: NiTi tube under bending: bending moment–end rotation response obtained for different combinations of dissipation parameters f_{c} and f_{r}.

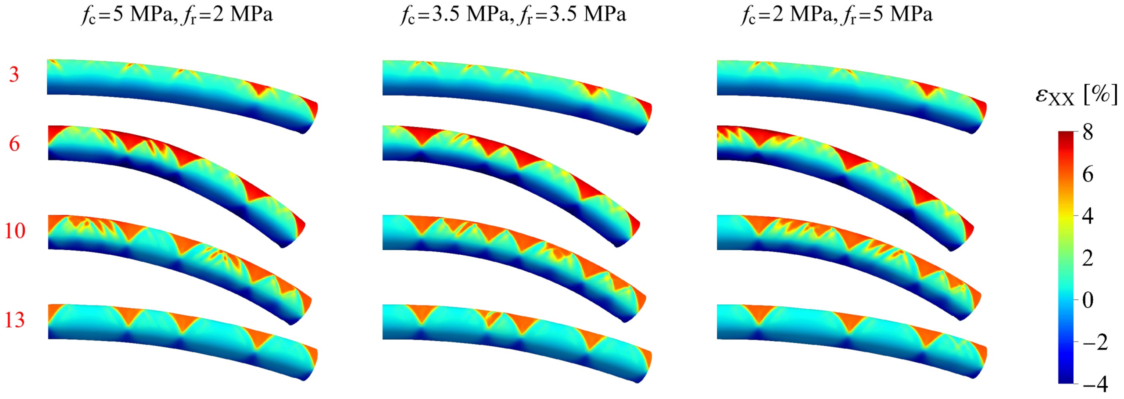

Figure 13: NiTi tube under bending: predicted transformation pattern for different combinations of dissipation parameters f_{c} and f_{r}. The numbers marking the snapshots correspond to the same end rotations as those indicated on the mechanical response in Fig. 8.

related computations are conducted for the half tube configuration. Given the proportional nature of the bending loading, it is expected that the martensite reorientation does not play a major role in shaping the phase transformation pathway, hence minimal qualitative impact of the reorientation dissipation. The results are illustrated in Figs. 12 and 13. It follows that the changes mainly manifest in the shape and amplitude of moment oscillations in the mechanical response as well as in the subtle details of the transformation morphology. However, identifying a systematic pattern of changes is likely infeasible.

4.4. Numerical study 3: on the striations of the transformation front

It has been frequently observed in the experiments involving NiTi straight/tube specimens under tension-dominated loading that faint striations[1] are left behind at the wake of a traveling phase transformation front, in particular when the front features a criss-cross pattern (as

---

[1] The term 'striations' is adopted here following the terminology of (Reedlunn et al., 2014, 2020).

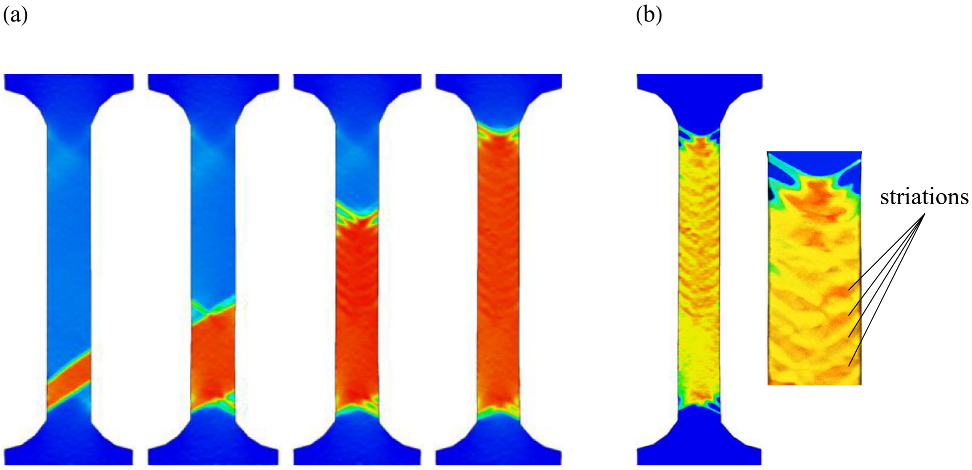

Figure 14: Phase transformation evolution recorded in the experiment of Shariat et al. (2022): (a) representative snapshots of the transformation pattern during loading and (b) details of the transformation pattern at the end of loading, displaying clearly the striations. In both panels, the transformation is represented by the axial strain field, however, the color scale used in panel (b) is manipulated to enhance the visibility of striations. The figure is reproduced with permission from Elsevier.

in straight samples) or a multi-pronged pattern (as in tube geometries) (Kim and Daly, 2011; Bechle and Kyriakides, 2014; Reedlunn et al., 2014, 2020; Shariat et al., 2022). Fig. 14, reproduced from Shariat et al. (2022), showcases the presence of front striations in a NiTi dog-bone specimen under tension. The revelation of striations has been facilitated by the use of Digital Image Correlation (DIC) technique, which unveils the very fine details of the transformation evolution pattern, although hints on their existence were noted in earlier studies that did not employ the DIC technique (Shaw and Kyriakides, 1997). Despite their ubiquitous presence, scant attention has been given to the origin and characteristics of striations. The general consensus is that striations represent regions of incompletely transformed martensite, which may eventually reach saturation at higher stresses. In our previous study (Rezaee-Hajidehi and Stupkiewicz, 2023), we argued that striations emerge as a result of a distinct evolution pathway within the front fingers and their surroundings, indicating a different evolution of the transformation strain. This implies that a model that accurately captures the evolution of the transformation strain can effectively describe the striations. In the present framework, this is made feasible by the incorporation of the martensite reorientation dissipation. In fact, the goal of this investigation is to highlight the role of martensite reorientation dissipation in predicting the striations.

The NiTi dog-bone specimen in the experiment of Shariat et al. (2022) was examined under isothermal uniaxial tension in a displacement-control loading mode. The dog-bone had a gauge length of $L_0 = 30$ mm, a gauge width of 5 mm and a thickness of 0.22 mm. The same setup is employed in this study. The dog-bone geometry is discretized uniformly within the gauge segment using elements of an in-plane size of 0.14 mm. To optimize the computational effort, only one element is used through the thickness. In addition, the mesh is made coarser within the clamping segments which do not participate in the transformation. Idealized boundary conditions are imposed: displacements at the bottom surface are fully constrained, while at the

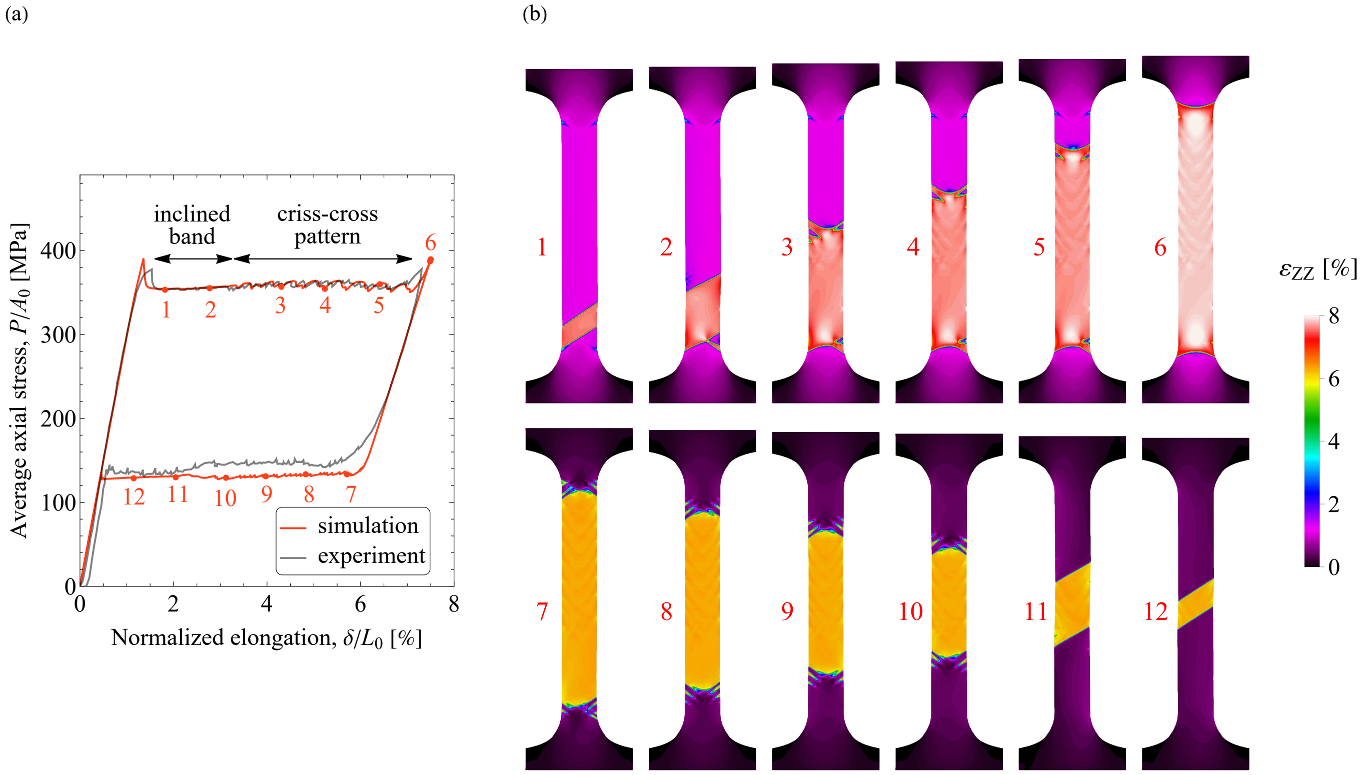

Figure 15: NiTi dog-bone under uniaxial tension: (a) mechanical response and (b) transformation pattern. The experimental response in panel (a) refers to Shariat et al. (2022), and the corresponding transformation pattern is depicted in Fig. 14.

top surface, lateral displacements are constrained and the axial displacement δ is prescribed. To provoke the localization of a single martensite band, a geometrical imperfection is placed at the bottom end of the gauge segment. The analysis begins by examining the case with the reference pair of dissipation parameters, $f_\mathrm{c} = f_\mathrm{r} = 3$ MPa, to establish a baseline for subsequent comparisons. The analysis is then extended to explore the impact of dissipation parameters on the evolution of striations.

Fig. 15 presents the mechanical responses alongside selected snapshots of the predicted transformation pattern during loading and unloading. The mechanical response is expressed in terms of the average axial stress P/A_0 versus the normalized elongation δ/L_0, with P and A_0 denoting the axial force and initial cross-section area, respectively. A rich color-scale is utilized for a vivid illustration of the transformation pattern, enabling a clear identification of the striations. The results show a strong correlation with the experimental counterpart, see Fig. 14 for the comparisons of the transformation patterns. Initially, the transformation features a single traveling inclined interface that persists until a normalized elongation of about 3% is reached. Afterwards, the front transitions into a criss-cross configuration characterized by alternating left-handed and right-handed fingers. As a consequence of this transition, the stress plateau in the mechanical response changes from a smooth appearance to a ragged appearance. During unloading, a similar front transitioning occurs in a reverse sequence, with the front initially adopting a criss-cross configuration, shrinking simultaneously from both ends,

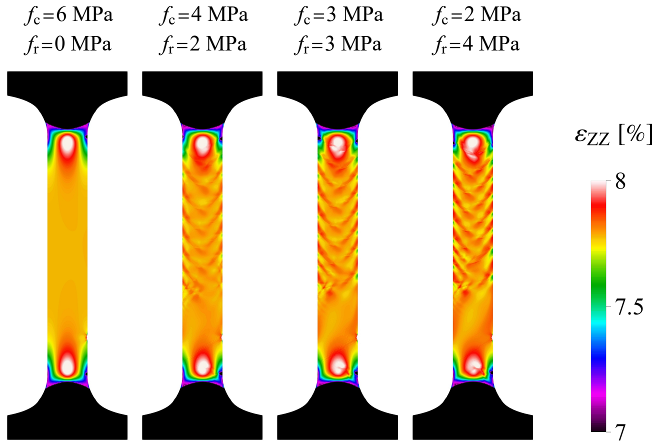

Figure 16: NiTi dog-bone under uniaxial tension: a more detailed look at the transformed domain at the end of loading for different combinations of the dissipation parameters f_c and f_r.

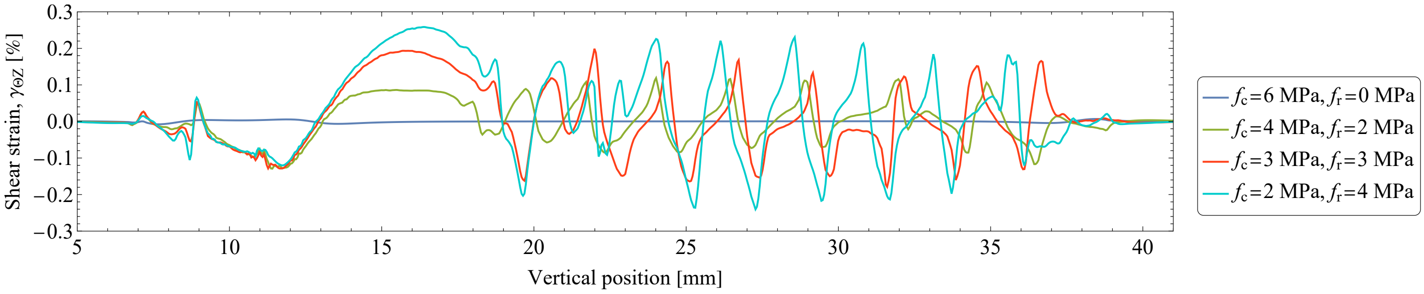

Figure 17: Distribution of the shear strain $\gamma_{\Theta Z}$ along the centerline of the dog-bone at the end of the loading stage. The plot corresponds to the gauge segment of the dog-bone.

that later reforms into inclined interfaces that persist for the remainder of the reverse transformation. Of particular importance is the manifestation of striations within the transformed domain that extend over the criss-cross route. Consistent with the experiment, striations exhibit an approximately 0.5% of higher axial strain with respect to the surroundings.

The striations form when a criss-cross propagation mode is active. The criss-cross propagation is a self-adjusting mechanism in response to the excessive misalignment of the specimen and the ensuing intolerable in-plane bending moment. The alternating arrangement of the criss-cross fingers acts as a corrective measure to straighten the specimen and mitigate the bending moment, as discussed by Shaw and Kyriakides (1997); Jiang et al. (2017b); Shariat et al. (2022). The right-handed and left-handed fingers are associated with shear strains of opposing directions, an observation which is in line with the experimental findings of Shariat et al. (2022), see Fig. 4 therein. Indeed, the formation of striations can be intuitively linked to the evolution of shear strains: the larger the shear strains, the more pronounced the striations. This is illustrated in Fig. 16 and 17 that compare, for different combinations of the dissipation parameters f_c and f_r, the transformed domain at the end of loading and the distribution of the shear strain $\gamma_{\Theta Z}$ along the centerline of the dog-bone, respectively. For a clear illustration in Fig. 16, the color scale covers only the highest 1% of axial strain ε_{ZZ}. It can be seen that as the dissipation parameter f_r increases, so does the amplitude of shear strain, and thereby,

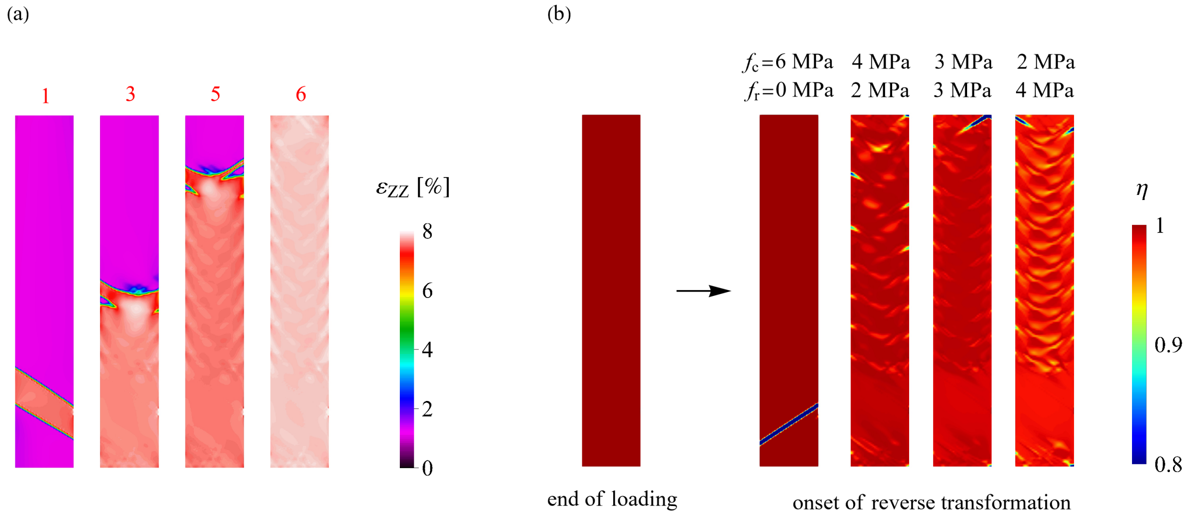

Figure 18: NiTi strip under uniaxial tension: (a) the transformation pattern during loading for the reference dissipation parameters $f_c = 3$ MPa and $f_r = 3$ MPa, and (b) the effect of the dissipation parameters f_c and f_r on the pattern of the martensite volume fraction at the onset of the reverse transformation during unloading. The numbers in panel (a) refer to the same overall elongations as those indicated in Fig. 15(a).

the striations become more pronounced. While, for $f_r = 0$ with no reorientation dissipation, shear strain is relatively negligible and no trace of striations is visible.

As discussed earlier in this section, striations are commonly perceived as areas of incomplete martensitic transformation. It is thus intriguing to examine the evolution of martensite volume fraction η within the zone of striations. Interestingly, results show no sign of non-uniformity of η within the zone of striations during loading. However, at the onset of reverse transformation during unloading, a non-uniform distribution of η becomes evident. The non-uniformity is insignificant and the related results are not explicitly reported here. To further investigate this aspect, another set of simulations are performed on a NiTi strip with material parameters identical to those of the dog-bone and dimensions equal to its gauge segment. The objective is to allow the transformation to spread throughout the entire specimen and analyze the potential impacts on the distribution of the martensite volume fraction η during unloading. To achieve this, less restrictive boundary conditions permitting lateral displacement of the strip are imposed. The corresponding results are presented in Fig. 18. Similar to the dog-bone, the transformation evolves in the form of a criss-cross pattern during loading, see Fig. 18(a). An interesting non-uniformity of η is observed that appears abruptly and immediately at the onset of of the reverse transformation, see Fig. 18(b). The non-uniformity adapts the pattern of striations and becomes more severe as the dissipation parameter f_r is increased. As a result of this non-uniformity, the reverse transformation consistently initiates from the top edge of the strip. In contrast, in the case of $f_r = 0$ with a uniform distribution of volume fraction η, the reverse transformation is triggered at the position of the imperfection.

The discussion concludes by noting that in addition to martensite reorientation dissipation, an intrinsic stress–strain response with an adequate nonlinearity within the transformation regime also contributes to the formation of striations. To further look into this, an additional simulation has been conducted with a nonlinear intrinsic response, similar to that employed in our previous study (Rezaee-Hajidehi and Stupkiewicz, 2023). As expected, the results reveal a non-uniform distribution of η within the striations zone during both loading and unloading. Striations are also, to some extent, affected, in terms of both the evolution pattern and the strain amplitude. For brevity, the corresponding snapshots are not reported here.

5. Conclusion

To reliably predict the phase transformation behavior under arbitrary loading conditions, it is crucial that the SMA constitutive model is capable of accurately capturing the evolution of the transformation strain. Specifically, the model must adequately account for the martensite reorientation effects. This necessity is further substantiated by the occurrence of transformation localization, as a result of which the material points undergo complex non-proportional stress/strain paths even under a macroscopically proportional loading. In light of these considerations, an advanced model of pseudoelasticity is developed in this work. The model extends the constitutive description proposed by Stupkiewicz and Petryk (2013). A new rate-independent dissipation potential is formulated that assigns dissipation to the evolution of martensite volume fraction and transformation strain. The finite-element implementation of the model relies on the augmented Lagrangian treatment of the non-smooth minimization problem. Thanks to the micromorphic regularization, the resulting computational complexities are taken care of efficiently at the local (integration-point) level.

The constitutive description of the model encompasses tension–compression asymmetry and transverse isotropy of the transformation strain. These features, along with the newly introduced dissipation potential, deliver a unique model of pseudoelasticity, capable of addressing a broad range of applications, including non-proportional loading conditions. In this regard, three numerical studies have been conducted and their outcomes are summarized below. (i) The model has successfully captured the complex stress response of the NiTi tube under non-proportional tension–torsion. In tension-then-torsion scenarios, where the transformation localization prevails, the predicted martensite reorientation effects are less pronounced compared to torsion-then-tension. (ii) The model has well reproduced the intriguing diamond-shaped phase transformation pattern of the NiTi tube subjected to pure bending. The simulated structural features were in a good agreement with the experimental findings of Bechle and Kyriakides (2014), especially when the ideal mid-point symmetry condition is not imposed. (iii) Lastly, the controlling role of the martensite reorientation on the striations of the transformation front has been pinpointed. The reorientation effects come into action due to the complex deformation path of the front fingers. This modeling study is apparently the first time that a detailed analysis is performed on the front striations.

Acknowledgement. The author wishes to thank Prof. Stanisław Stupkiewicz from IPPT PAN for helpful discussions on the model formulation and results. This work has been supported by the National Science Centre (NCN) in Poland through the Grant No. 2021/43/D/ST8/02555. For the purpose of Open Access, the author has applied a CC-BY public copyright license to any Author Accepted Manuscript (AAM) version arising from this submission.

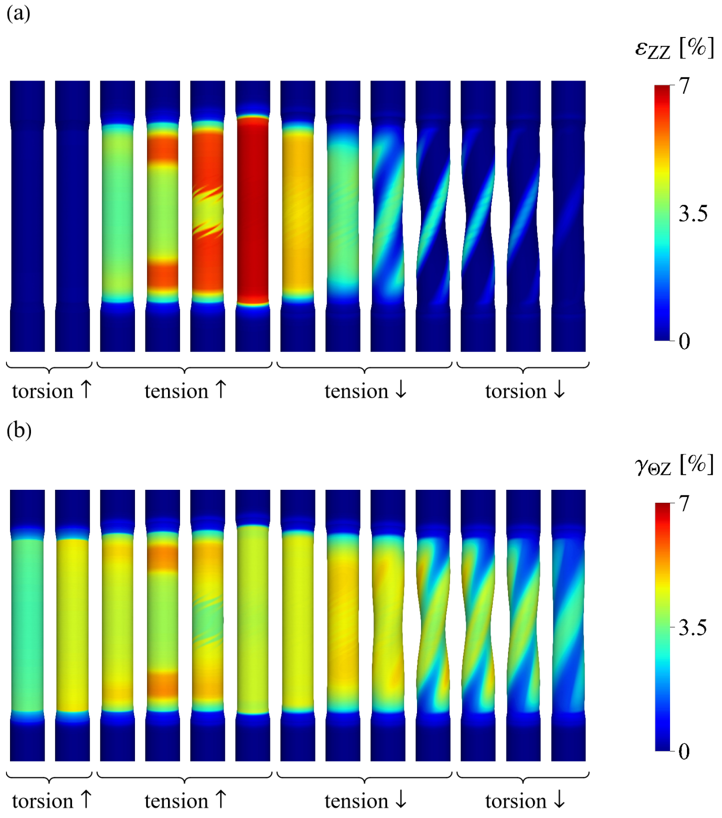

Figure A.1: NiTi tube under torsion (4%) followed by tension (6%) exhibiting helical buckling: snapshots of the axial strain field ε_{ZZ} (a) and shear strain field $\gamma_{\Theta Z}$ (b) for the simulation with the dissipation parameters $f_c = 3$ MPa and $f_r = 3$ MPa.

Appendix A. NiTi tube under torsion-then-tension: occurrence of helical buckling

A curious result emerged in the study in Section 4.2: the tube unexpectedly buckled when subjected to 4% torsion followed by 6% tension. This buckling was not reported in the experiment of McNaney et al. (2003), and interestingly, it occurred during unloading. In this appendix, the results of the buckled tube are briefly discussed.

Figs. A.1 and A.2 depict the snapshots of the deformed tube configuration overlaid with contours of axial and shear strain fields, and the mechanical response of the tube, respectively. Upon comparing the phase transformation evolution with that of the thicker tube in the reference simulation (see Fig. 7), it becomes apparent that the transformation evolutions are identical until more than halfway through tensile unloading. It is at this point, at about an axial strain of $\varepsilon = 2\%$, that the tube experiences a buckling instability, in the form of a helical deformation. Accompanied by this, the equivalent stress σ_{eq} declines, which eventually results in a noticeable bump shape in the mechanical response.

A peculiar observation in this analysis is that the helical buckling does occur during unloading. A closer inspection of the transformation pattern reveals that a mild phase transformation inhomogeneity still exists at the onset of helical buckling, which may have stimulated the buckling. It is also worthwhile to mention that the finite-element simulations of the tube

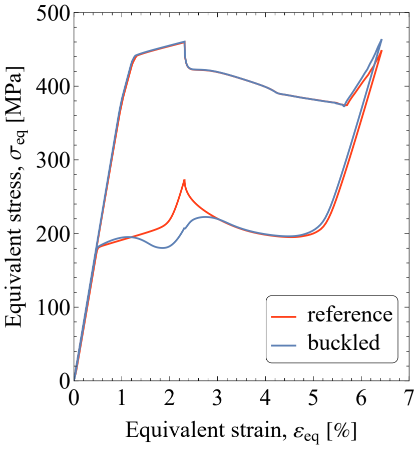

Figure A.2: NiTi tube under torsion (4%) followed by tension (6%): comparison of the mechanical responses for the reference case and the case that exhibits buckling. The reference case is the one for the thicker tube analyzed in Section 4.2.

involve certain simplifications compared to real experimental conditions. Notable among them is the absence of residual stresses that are typically present in drawn tubes. As discussed by Rodríguez and Merodio (2016), depending on the magnitude of the residual stresses and the sign of the eigenstrains they induce, helical buckling can be promoted or hindered. Nevertheless, an in-depth analysis of the helical buckling is not pursued here, as it falls beyond the scope of the current study.

References

Alarcon, E., Heller, L., Arbab Chirani, S., Šittner, P., Kopeček, J., Saint-Sulpice, L., Calloch, S., 2017. Fatigue performance of superelastic NiTi near stress-induced martensitic transformation. Int. J. Fatigue 95, 76–89.

Alart, P., Curnier, A., 1991. A mixed formulation for frictional contact problems prone to newton like solution methods. Comp. Meth. Appl. Mech. Engng. 92, 353–375.

Alsawalhi, M.Y., Landis, C.M., 2022. A new phenomenological constitutive model for shape memory alloys. Int. J. Solids Struct. 257, 111264.

Auricchio, F., Bonetti, E., Scalet, G., Ubertini, F., 2014. Theoretical and numerical modeling of shape memory alloys accounting for multiple phase transformations and martensite reorientation. Int. J. Plast. 59, 30–54.

Barrera, N., Biscari, P., Urbano, M.F., 2014. Macroscopic modeling of functional fatigue in shape memory alloys. European Journal of Mechanics-A/Solids 45, 101–109.

Bechle, N.J., Kyriakides, S., 2014. Localization in NiTi tubes under bending. Int. J. Solids Struct. 51, 967–980.

Bhattacharya, K., 2003. Microstructure of martensite: why it forms and how it gives rise to the shape-memory effect. Oxford University Press, Oxford.

Bouvet, C., Calloch, S., Lexcellent, C., 2002. Mechanical behavior of a Cu-Al-Be shape memory alloy under multiaxial proportional and nonproportional loadings. J. Eng. Mater. Tech. 124, 112–124.

Cissé, C., Zaki, W., Ben Zineb, T., 2016. A review of constitutive models and modeling techniques for shape memory alloys. Int. J. Plast. 76, 244–284.

Duerig, T.W., Melton, K.N., Stöckel, D., Wayman, C.M., 2013. Engineering aspects of shape memory alloys. Butterworth-heinemann.

Forest, S., 2009. Micromorphic approach for gradient elasticity, viscoplasticity, and damage. J. Eng. Mech. 135, 117–131.

Frost, M., Benešová, B., Seiner, H., Kružík, M., Šittner, P., Sedlák, P., 2021. Thermomechanical model for NiTi-based shape memory alloys covering macroscopic localization of martensitic transformation. Int. J. Solids Struct. 221, 117–129.

Grabe, C., Bruhns, O.T., 2009. Path dependence and multiaxial behavior of a polycrystalline NiTi alloy within the pseudoelastic and pseudoplastic temperature regimes. Int. J. Plast. 25, 513–545.

Hallai, J.F., Kyriakides, S., 2011. On the effect of Lüders bands on the bending of steel tubes. Part II: Analysis. Int. J. Solids Struct. 48, 3285–3298.

Hallai, J.F., Kyriakides, S., 2013. Underlying material response for Lüders-like instabilities. Int. J. Plast. 47, 1–12.

He, Y.J., Sun, Q.P., 2009. Effects of structural and material length scales on stress-induced martensite macro-domain patterns in tube configurations. Int. J. Solids Struct. 46, 3045–3060.

He, Y.J., Sun, Q.P., 2010. Macroscopic equilibrium domain structure and geometric compatibility in elastic phase transition of thin plates. Int. J. Mech. Sci. 52, 198–211.

Helm, D., Haupt, P., 2003. Shape memory behaviour: modelling within continuum thermomechanics. Int. J. Solids Struct. 40, 827–849.

Holzapfel, G.A., 2006. Nonlinear Solid Mechanics. Wiley, Chichester.

Jiang, D., Kyriakides, S., Bechle, N.J., Landis, C.M., 2017a. Bending of pseudoelastic NiTi tubes. Int. J. Solids Struct. 124, 192–214.

Jiang, D., Kyriakides, S., Landis, C.M., Kazinakis, K., 2017b. Modeling of propagation of phase transformation fronts in NiTi under uniaxial tension. Eur. J. Mech. A/Solids 64, 131–142.

Kazinakis, K., Kyriakides, S., Jiang, D., Bechle, N.J., Landis, C.M., 2021. Buckling and collapse of pseudoelastic NiTi tubes under bending. Int. J. Solids Struct. 221, 2–17.

Kim, K., Daly, S., 2011. Martensite strain memory in the shape memory alloy nickel-titanium under mechanical cycling. Exp. Mech. 51, 641–652.

Korelc, J., 2009. Automation of primal and sensitivity analysis of transient coupled problems. Comp. Mech. 44, 631–649.

Korelc, J., Wriggers, P., 2016. Automation of Finite Element Methods. Springer International Publishing, Switzerland.

Lagoudas, D.C., Entchev, P.B., Popov, P., Patoor, E., Brinson, L.C., Gao, X., 2006. Shape memory alloys, Part II: Modeling of polycrystals. Mech. Mat. 38, 430–462.

Lim, T.J., McDowell, D.L., 1999. Mechanical behavior of an Ni-Ti shape memory alloy under axial-torsional proportional and nonproportional loading. J. Eng. Mater. Tech. 121, 9–18.

Luig, P., Bruhns, O.T., 2008. On the modeling of shape memory alloys using tensorial internal variables. Mat. Sci. Engng. A 481, 379–383.

Mazière, M., Forest, S., 2015. Strain gradient plasticity modeling and finite element simulation of Lüders band formation and propagation. Continuum Mech. Thermodyn. 27, 83–104.

McNaney, J.M., Imbeni, V., Jung, Y., Papadopoulos, P., Ritchie, R.O., 2003. An experimental study of the superelastic effect in a shape-memory Nitinol alloy under biaxial loading. Mech. Mat. 35, 969–986.

Miehe, C., 2011. A multi-field incremental variational framework for gradient-extended standard dissipative solids. J. Mech. Phys. Solids 59, 898–923.

Miyazaki, S., Otsuka, K., Wayman, C., 1989. The shape memory mechanism associated with the martensitic transformation in Ti–Ni alloys—II. Variant coalescence and shape recovery. Acta Metall. 37, 1885–1890.

Petrini, L., Bertini, A., 2020. A three-dimensional phenomenological model describing cyclic behavior of shape memory alloys. Int. J. Plast. 125, 348–373.

Petryk, H., 2003. Incremental energy minimization in dissipative solids. C. R. Mecanique 331, 469–474.

Pietrzak, G., Curnier, A., 1999. Large deformation frictional contact mechanics: continuum formulation and augmented lagrangian treatment. Comp. Meth. Appl. Mech. Engng. 177, 351–381.

Reedlunn, B., Churchill, C.B., Nelson, E.E., Shaw, J.A., Daly, S.H., 2014. Tension, compression, and bending of superelastic shape memory alloy tubes. J. Mech. Phys. Solids 63, 506–537.

Reedlunn, B., LePage, W.S., Daly, S.H., Shaw, J.A., 2020. Axial-torsion behavior of superelastic tubes: Part I, proportional isothermal experiments. Int. J. Solids Struct. 199, 1–35.

Rezaee Hajidehi, M., Stupkiewicz, S., 2018. Gradient-enhanced model and its micromorphic regularization for simulation of Lüders-like bands in shape memory alloys. Int. J. Solids Struct. 135, 208–218.

Rezaee-Hajidehi, M., Stupkiewicz, S., 2021a. Micromorphic approach to phase-field modeling of multivariant martensitic transformation with rate-independent dissipation effects. Int. J. Solids Struct. 222, 111027.

Rezaee-Hajidehi, M., Stupkiewicz, S., 2021b. Modelling of propagating instabilities in pseudoelastic NiTi tubes under combined tension–torsion: helical bands and apparent yield locus. Int. J. Solids Struct. 221, 130–149.

Rezaee-Hajidehi, M., Stupkiewicz, S., 2023. Predicting transformation patterns in pseudoelastic NiTi tubes under proportional axial–torsion loading. Int. J. Solids Struct. 281, 112436.

Rezaee-Hajidehi, M., Tůma, K., Stupkiewicz, S., 2020. Gradient-enhanced thermomechanical 3D model for simulation of transformation patterns in pseudoelastic shape memory alloys. Int. J. Plast. 128, 102589.

Rodríguez, J., Merodio, J., 2016. Helical buckling and postbuckling of pre-stressed cylindrical tubes under finite torsion. Finite Elem. Anal. Des. 112, 1–10.

Saleeb, A.F., Padula II, S.A., Kumar, A., 2011. A multi-axial, multimechanism based constitutive model for the comprehensive representation of the evolutionary response of SMAs under general thermomechanical loading conditions. Int. J. Plast. 27, 655–687.

Sedlak, P., Frost, M., Benešová, B., Ben Zineb, T., Šittner, P., 2012. Thermomechanical model for NiTi-based shape memory alloys including R-phase and material anisotropy under multiaxial loadings. Int. J. Plast. 39, 132–151.

Shariat, B.S., Li, Y., Yang, H., Wang, Y., Liu, Y., 2022. Shear strain evolution during tension-induced Lüders-type deformation of polycrystalline NiTi plates. Mat. Sci. Engng. A 839, 142774.

Shaw, J.A., Kyriakides, S., 1997. Initiation and propagation of localized deformation in elasto-plastic strips under uniaxial tension. Int. J. Plast. 13, 837–871.

Song, D., Kang, G., Kan, Q., Yu, C., Zhang, C., 2014. Non-proportional multiaxial transformation ratchetting of super-elastic NiTi shape memory alloy: Experimental observations. Mech. Mat. 70, 94–105.

Stupkiewicz, S., Petryk, H., 2013. A robust model of pseudoelasticity in shape memory alloys. Int. J. Num. Meth. Engng. 93, 747–769.

Sun, Q.P., He, Y.J., 2008. A multiscale continuum model of the grain-size dependence of the stress hysteresis in shape memory alloy polycrystals. Int. J. Solids Struct. 45, 3868–3896.

Sun, Q.P., Li, Z.Q., 2002. Phase transformation in superelastic NiTi polycrystalline micro-tubes under tension and torsion—from localization to homogeneous deformation. Int. J. Solids Struct. 39, 3797–3809.

Wang, J., Moumni, Z., Zhang, W., 2017. A thermomechanically coupled finite-strain constitutive model for cyclic pseudoelasticity of polycrystalline shape memory alloys. Int. J. Plast. 97, 194–221.

Watkins, R.T., Reedlunn, B., Daly, S., Shaw, J.A., 2018. Uniaxial, pure bending, and column buckling experiments on superelastic NiTi rods and tubes. Int. J. Solids Struct. 146, 1–28.

Wendler, F., Ossmer, H., Chluba, C., Quandt, E., Kohl, M., 2017. Mesoscale simulation of elastocaloric cooling in SMA films. Acta Mater. 136, 105–117.

Yu, H., Landis, C.M., 2023. A gradient regularized model for shape memory alloys. Mech. Mat. 183, 104689.

Zhang, X., Feng, P., He, Y., Yu, T., Sun, Q.P., 2010. Experimental study on rate dependence of macroscopic domain and stress hysteresis in NiTi shape memory alloy strips. Int. J. Mech. Sci. 52, 1660–1670.